

DEDALUS - Acervo - ICMSC



30300031381

---

**A Front-Tracking Finite Difference Method to  
Solve the 3D Navier-Stokes Equations for  
Multi-Fluid Flows with Free Surfaces**

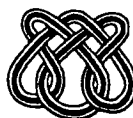
**Fabrício Simeoni Sousa  
Norberto Mangiavacchi  
Luis Gustavo Nonato  
Antonio Castelo Filho  
Murilo Francisco Tomé  
Valdemir Garcia Ferreira  
José Alberto Cuminato  
Sean McKee**

**Nº 73**

---

**NOTAS**

**Série Computação**



**São Carlos – SP  
Ago./2003**

# A Front-tracking Finite Difference Method to solve the 3D Navier-Stokes equations for Multi-Fluid Flows with Free Surfaces

Fabrício Simeoni Sousa<sup>a</sup>, Norberto Mangiavacchi<sup>b</sup>,  
Luis Gustavo Nonato<sup>a</sup>, Antonio Castelo Filho<sup>a</sup>,  
Murilo Francisco Torné<sup>a</sup>, Valdemir Garcia Ferreira<sup>a</sup>,  
José Alberto Cuminato<sup>a</sup>, Sean McKee<sup>c</sup>

<sup>a</sup>*Departamento de Ciências de Computação e Estatística.  
Instituto de Ciências Matemáticas e de Computação – USP,  
São Carlos, SP, Brasil.*

<sup>b</sup>*Departamento de Engenharia Mecânica  
Universidade do Estado do Rio de Janeiro,  
Rio de Janeiro, RJ, Brasil.*

<sup>c</sup>*Department of Mathematics  
University of Strathclyde,  
Scotland, UK.*

---

## Abstract

A method for simulating incompressible, immiscible, Newtonian, unsteady, multi-fluid flows with free surfaces is described. A sharp interface separates fluids of different density and viscosity. Surface and interfacial tensions are also considered and the required curvature is geometrically approximated at the fronts by a least squares quadratic fitting [4]. To remove small undulations at the fronts, a mass-conserving filter is employed. The numerical method employed to solve the Navier-Stokes equations is based on the GENSMAC-3D [28] front-tracking method. The velocity field is computed using a finite-difference scheme on an Eulerian grid. The free-surface and the interfaces are represented by an unstructured Lagrangian grid moving through an Eulerian grid. The method was validated by comparing the numerical results with analytical results for a number of simple problems. Complex numerical simulations show the capability and emphasize the robustness of this new method.

## Resumo

Neste trabalho é apresentado um novo método para simular escoamentos incompressíveis multifásicos de fluidos imiscíveis e Newtonianos, com superfícies livres. São consideradas tensões superficial e interfacial, onde a curvatura necessária para os cálculos é aproximada geometricamente nas fronteiras livres por um método de mínimos quadrados [4]. Para remover pequenas ondulações nas fronteiras livres, foi utilizado um filtro que reposiciona as partículas marcadoras da superfície, conservando a massa do fluido. O método numérico para solução das equações de Navier-Stokes foi baseado no método GENSMAC-3D [28], utilizando o método de front-tracking para representação das fronteiras livres. O campo de velocidades é calculado utilizando um esquema de diferenças finitas em uma malha Euleriana, e a superfície livre e interfaces são representadas por malhas Lagrangianas não estruturadas, movendo-se sobre a malha Euleriana. O método foi validado comparando-se os resultados numéricos com soluções analíticas de problemas conhecidos. Simulações mais complexas mostram as capacidades e enfatizam a robustez deste novo método.

---

*Key words:* Front-tracking method, Multi-fluid flows, Numerical simulation, Surface tension, Free surface flows, Finite Difference Method

---

## 1 Introduction

Numerical simulations of fluid flows are relevant to problems found in various industries such as oil, nuclear, chemical and the food industry. Applications involving flows of several fluids, called multi-fluid flows, include heavy oil transport, food processing, co-extrusion, bubble flows and so. If the fluid involves both gas and liquid, the fluid is referred to as two-phase.

Multi-fluid flows are complicated because of the many physical phenomena that need to be taken into account. Prime among these is surface or interfacial tension between any two fluids. This can be particularly difficult when the two fluids are very different: a simple example is that of bubbles in water, where the density ratio is about 1000 to 1.

There are essential two techniques for approximating the interface: *front capturing* and *front tracking*. Front capturing techniques are characterized by treating the interface as a high variation region with no explicit elements to represent the interface. With this approach it is arguably easier to deal with topological changes in the interface (or interfaces) like merging and breaking. However, a major disadvantage of this technique is the interface diffusion over several cells, resulting in loss of precision.

Early work on front capturing goes back to Glimm and his co-workers (see, eg Glimm et al. [10]) where they represented the moving front by a connected set of points which form a moving internal boundary. An irregular grid is then constructed in order to calculate the evolution of the fluid in the vicinity of the interface. A special finite difference is then employed on the irregular grid. More recently the level set approach [25] has found prominence. This approach employs a smooth function  $\phi$ , called the level set function, to represent the free surface. Liquid regions are regions which have  $\phi(\mathbf{x}, t) > 0$  while the region containing the other fluid are regions in which  $\phi(\mathbf{x}, t) < 0$ . The free surface is the set of points such that  $\phi(\mathbf{x}, t) = 0$ . The unit normal and the mean curvature are then easily computed. They are given by

$$\mathbf{n} = \frac{\nabla\phi}{|\nabla\phi|} \quad \text{and} \quad \kappa = \nabla \cdot \frac{\nabla\phi}{|\nabla\phi|},$$

respectively. This method was introduced by Osher and Sethian [18], and strongly promoted in two books by Sethian [20,21].

Essentially front tracking involves explicit computational elements moving through a (static) Eulerian grid. This approach can be more accurate than the above, but can require additional computational resources. Furthermore, to take into account topological changes in the interface, the implementation can become more complex. A front tracking method has been described by Tryggvason and his co-workers [7,8,32] in which the interface (or interfaces) are considered to be a linked set of points forming an unstructured mesh. This unstructured mesh moves through a staggered Eulerian grid upon which the fluid velocity and pressure are calculated.

The *Marker-and-Cell* (MAC) method was first introduced by Harlow and Welch [11]. It was specifically designed for calculating incompressible viscous free surface flows. It is a finite difference method based on a staggered grid that employs the primitive variables of velocity and pressure. Due to computational difficulties, Amsden and Harlow [1] developed a projection method called *Simplified Marker-and-Cell* (SMAC) whereby essentially the velocity and pressure field are calculated sequentially. In the years that followed many people have studied and worked on the SMAC method (eg Armenio [2], Hirt and Nichols [12], Miyata [15], Viecelli [34] and Veldman and Vogels [33] ). More recently, and motivated by the SMAC philosophy, Tomé and McKee [26] developed the GENSMAC method for two dimensional incompressible viscous fluids with free surfaces in an arbitrary complex domain. A three-dimensional version of this method, called GENSMAC-3D [28], extended this work.

The starting point for this work is the GENSMAC-3D [26,28] method. However, rather than dealing with a single fluid, we shall be concerned with an arbitrary number of Newtonian fluids with different densities and viscosities, all separated by interfaces which must be determined. In addition there is also a free surface or free surfaces that must be treated. The fronts, both free surface and interfaces, will lie on Lagrangian meshes that will move through an Eulerian grid on which the fluid velocity and pressure will be calculated. The approach is similar to Esmaeeli and Tryggvason [7,8], but there are significant differences, both in the discretization employed and in the way in which the interfacial forces are calculated. Both the normal to the surface and its curvature are required. However, before these may be calculated it is necessary to remove sub-cell undulations. Thus the technique for determinig the normal and the curvature is two-stage: a novel technique for sub-cell undulations removal is followed by the calculation of the normal and the curvature.

## 2 Formulation and numerical method

The governing equations for incompressible flows are the Navier-Stokes equations. The approach used here is to consider the density and viscosity as variables over the whole domain, but constant in each specific fluid. Thus, each fluid is taken to be incompressible, and the continuity equation is valid over the whole domain.

When taking into account the interfacial tension forces and the fact that the density and the viscosity are variable over the whole region, the nondimensional momentum equation is given by

$$\begin{aligned} \frac{\partial \mathbf{u}}{\partial t} + \nabla \cdot (\mathbf{u}\mathbf{u}) &= -\frac{1}{\rho} \nabla p + \frac{1}{\rho Re} \nabla \cdot \mu(\nabla \mathbf{u} + \nabla \mathbf{u}^T) + \frac{1}{Fr^2} \mathbf{g} \\ &+ \frac{1}{\rho We} \int \sigma_I \kappa' \mathbf{n}' \delta^\beta(\mathbf{x} - \mathbf{x}') dS' \end{aligned} \quad (1)$$

where  $\mathbf{u} = \mathbf{u}(\mathbf{x}, t)$  denotes the velocity field,  $p = p(\mathbf{x}, t)$  is the pressure field,  $\rho = \rho(\mathbf{x}, t)$  and  $\mu = \mu(\mathbf{x}, t)$  are the density and viscosity fields of the fluid all in nondimensional form. Here  $\mathbf{g}$  denotes the gravitational field. Furthermore,  $Re = \rho_0 LU / \mu_0$ ,  $Fr = U / \sqrt{Lg}$  and  $We = \rho_0 LU^2 / \sigma_0$  denotes the Reynolds number, the Froude number and the Weber number, respectively. Here,  $L$  and  $U$  are the length and velocity scales,  $\rho_0$ ,  $\mu_0$  and  $\sigma_0$  are the reference values of density, viscosity and surface tension, and  $g$  denotes the gravitational constant. The interfacial force term in the momentum equation

$$\frac{1}{\rho We} \int \sigma_I \kappa' \mathbf{n}' \delta^\beta(\mathbf{x} - \mathbf{x}') dS' \quad (2)$$

was proposed by Esmaeeli and Tryggvason [7,8], where  $\sigma_I$  is the nondimensional interfacial tension coefficient,  $\kappa$  is the curvature,  $\mathbf{n}$  is the normal vector and  $\delta^\beta(\mathbf{x} - \mathbf{x}')$  is a  $\beta$ -dimensional  $\delta$ -function, constructed by repeated multiplication of one-dimensional  $\delta$ -functions. For example, for  $\beta = 3$  we have

$$\delta^3(\mathbf{x} - \mathbf{x}') = \delta(x - x')\delta(y - y')\delta(z - z'), \quad (3)$$

where  $\mathbf{x} = (x, y, z)$  and  $\mathbf{x}' = (x', y', z')$ . The primed variables are computed on the interface. The surface integral in (1) and (2) are evaluated over all the interfaces.

In this work an alternative form of the interface force term will be used. Let  $H : \mathbb{R}^3 \rightarrow \{0, 1\}$  be a *Heaviside* function, which can be defined as being 1 in the interior of a specific fluid and 0 otherwise. Let  $V(t)$  be a time dependent three-dimensional

volume with its surface denoted by  $S(t)$ . The Heaviside function can be defined [29] as

$$H(x, y, z, t) = \int_{V(t)} \delta(x - x')\delta(y - y')\delta(z - z') dV'. \quad (4)$$

We are interested in the gradient of  $H$

$$\nabla H = \nabla \int_V [\delta(x - x')\delta(y - y')\delta(z - z')] dV', \quad (5)$$

where for brevity of notation, the dependence of  $t$  has been dropped. Notice that the gradient operator is with respect to the unprimed variables, and this operator may be permuted with the integral operator,

$$\nabla H = \int_V \nabla [\delta(x - x')\delta(y - y')\delta(z - z')] dV'. \quad (6)$$

Moreover, notice that the  $\delta$ -functions are antisymmetric with relation to the unprimed and primed variables (this follows directly from the chain rule). We may therefore write

$$\nabla H = - \int_V \nabla' [\delta(x - x')\delta(y - y')\delta(z - z')] dV', \quad (7)$$

and so, by using a variant of the divergence theorem, we obtain

$$\nabla H = - \oint_S \delta(x - x')\delta(y - y')\delta(z - z') \mathbf{n}' dS'. \quad (8)$$

In these equations, it was assumed that the volume occupied by the fluid is finite so that  $S$  is a closed contour. Notice that the contribution of most of the integral is zero so we can replace it by one over a part of the contour and hence write [29]:

$$\nabla H = - \int_S \delta(x - x')\delta(y - y')\delta(z - z') \mathbf{n}' dS'. \quad (9)$$

Thus the interface can be identified as the region where  $\nabla H$  is nonzero.

Finally, by using this property of the  $\delta$ -function under the integral sign, the interfacial force term can be written as

$$\mathbf{f} = \frac{1}{\rho We} \int \sigma_I \kappa' \mathbf{n}' \delta^\beta(\mathbf{x} - \mathbf{x}') dS' = - \frac{\sigma_I \kappa}{\rho We} \nabla H, \quad (10)$$

and the Navier-Stokes equations then take the form

$$\frac{\partial \mathbf{u}}{\partial t} + \nabla \cdot (\mathbf{u}\mathbf{u}) = -\frac{1}{\rho} \nabla p + \frac{1}{\rho Re} \nabla \cdot \mu(\nabla \mathbf{u} + \nabla \mathbf{u}^T) + \frac{1}{Fr^2} \mathbf{g} - \frac{\sigma_I \kappa}{\rho We} \nabla H. \quad (11)$$

All the fluids are assumed to be incompressible, so the velocity field is divergence free, that is

$$\nabla \cdot \mathbf{u} = 0. \quad (12)$$

Equations (11) and (12) are solved based on the GENSMAC-3D method [28], using an extension of the methodology described in [19] for the two-dimensional case. It is supposed that the velocity field  $\mathbf{u}(\mathbf{x}, t_0)$  is known at a given time  $t_0$ , and the boundary conditions for the velocity and pressure are given. The updated velocity field  $\mathbf{u}(\mathbf{x}, t)$ , at  $t = t_0 + \Delta t$ , is calculated using the following algorithm:

- (1) Let  $\tilde{p}(\mathbf{x}, t)$  be a pressure field which satisfies the correct pressure conditions on the free surface. This pressure field is computed according to the required boundary stress conditions.
- (2) The intermediate velocity field  $\tilde{\mathbf{u}}(\mathbf{x}, t)$  is computed by the explicitly discretized form of the momentum equations

$$\begin{aligned} \frac{\partial \tilde{\mathbf{u}}}{\partial t} + \nabla \cdot (\mathbf{u}\mathbf{u}) &= -\frac{1}{\rho} \nabla \tilde{p} + \frac{1}{\rho Re} \nabla \cdot \mu(\nabla \mathbf{u} + \nabla \mathbf{u}^T) \\ &+ \frac{1}{Fr^2} \mathbf{g} - \frac{\sigma_I \kappa}{\rho We} \nabla H \end{aligned} \quad (13)$$

with  $\tilde{\mathbf{u}}(\mathbf{x}, t_0) = \mathbf{u}(\mathbf{x}, t_0)$  using the correct boundary conditions for  $\mathbf{u}(\mathbf{x}, t_0)$ . It can be shown in [26] that  $\tilde{\mathbf{u}}(\mathbf{x}, t)$  possesses the correct vorticity at time  $t$ . However,  $\tilde{\mathbf{u}}(\mathbf{x}, t)$  does not satisfy (12). Let

$$\mathbf{u}(\mathbf{x}, t) = \tilde{\mathbf{u}}(\mathbf{x}, t) - \frac{1}{\rho} \nabla \psi(\mathbf{x}, t) \quad (14)$$

with

$$\nabla \cdot \frac{1}{\rho} \nabla \psi(\mathbf{x}, t) = \nabla \cdot \tilde{\mathbf{u}}(\mathbf{x}, t). \quad (15)$$

Thus,  $\mathbf{u}(\mathbf{x}, t)$  now satisfies (12) and the vorticity remains unchanged. Therefore,  $\mathbf{u}(\mathbf{x}, t)$  is identified as the updated velocity field at time  $t$ .

- (3) Solve the elliptic equation (15).
- (4) Compute the velocity by (14).

(5) Compute the pressure using

$$p(\mathbf{x}, t) = \tilde{p}(\mathbf{x}, t) + \frac{\psi(\mathbf{x}, t)}{\Delta t} . \quad (16)$$

(6) Update the positions of the marker particles.

The last step in the calculation involves moving the marker particles to their new positions. These are virtual particles whose coordinates are stored and updated at the end of each cycle by solving  $d\mathbf{x}/dt = \mathbf{u}$  by Euler's method. This provides the new coordinates of every particle, allowing us to determine whether or not it has moved to a new computational cell or if it has left the containment region through an outlet. Using the front-tracking methodology [28,32], only marker particles on the free surface and the interfaces need to be considered.

For the solution of (13), appropriate boundary conditions are required. At solid walls null velocities are enforced. At the free surface, the boundary conditions for pressure and velocity, assuming zero viscous stress in the empty phase, are given by

$$(\mathbf{S} \cdot \mathbf{n}) \cdot \mathbf{n} = p_{cap}, \quad (\mathbf{S} \cdot \mathbf{n}) \cdot \mathbf{m}_1 = 0, \quad (\mathbf{S} \cdot \mathbf{n}) \cdot \mathbf{m}_2 = 0 \quad (17)$$

where  $\mathbf{n}$ ,  $\mathbf{m}_1$  and  $\mathbf{m}_2$  are the local normal and tangential vectors to the free surface.  $\mathbf{S}$  is the viscous stress tensor, given by

$$\mathbf{S} = -p\mathbf{I} + \frac{\mu}{Re} [(\nabla\mathbf{u}) + (\nabla\mathbf{u})^T], \quad (18)$$

and  $p_{cap} = \sigma\kappa/We$  is the capillary pressure, originating from the effects of the surface tension  $\sigma$ . The elliptic equation (15) is solved using the conjugate gradient method, satisfying homogeneous Dirichlet boundary conditions at the free surface and homogeneous Neumann boundary conditions at the solid boundaries. However, as the density variation across the interface increases, more iterations are required for the convergence of the method. In these cases, a diagonal preconditioner was used to speed-up the convergence of the conjugate gradient method.

### 3 Discretizations

In a similar manner to MAC [35], SMAC [1] and GENSMAC [26] methods, equations (13)–(15) are discretized by finite differences on a staggered grid. Figure 1 shows an example of a staggered grid cell and the position of the variables in this

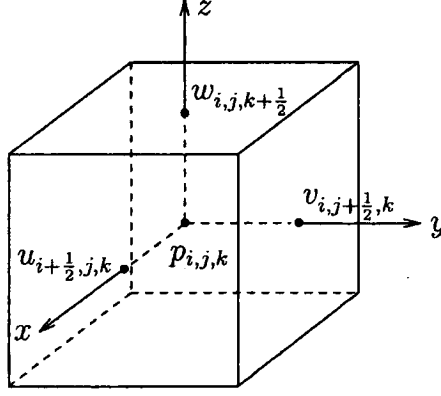


Fig. 1. Position of the variables in a cell. The velocities are computed on the faces of the cell, and the pressure ( $p$ ), density ( $\rho$ ), viscosity ( $\mu$ ) evaluated at the cell center.

cell: the velocities are calculated on the faces, and the other variables (pressure, density and viscosity) are computed at the cell center.

Consider the  $x$  component of the nondimensional momentum equation, expressed in Cartesian coordinates

$$\begin{aligned} \frac{\partial u}{\partial t} + \frac{\partial(u^2)}{\partial x} + \frac{\partial(uv)}{\partial y} + \frac{\partial(uw)}{\partial z} &= -\frac{1}{\rho} \frac{\partial p}{\partial x} + \frac{\mu}{\rho Re} \left( \frac{\partial^2 u}{\partial x^2} + \frac{\partial^2 u}{\partial y^2} + \frac{\partial^2 u}{\partial z^2} \right) \\ &+ \frac{1}{\rho Re} \left[ 2 \frac{\partial \mu}{\partial x} \frac{\partial u}{\partial x} + \frac{\partial \mu}{\partial y} \left( \frac{\partial v}{\partial x} + \frac{\partial u}{\partial y} \right) + \frac{\partial \mu}{\partial z} \left( \frac{\partial w}{\partial x} + \frac{\partial u}{\partial z} \right) \right] \\ &+ \frac{1}{Fr^2} g_x - \frac{\sigma_I \kappa}{\rho We} \frac{\partial H}{\partial x}. \end{aligned} \quad (19)$$

This equation can be written in the compact form,

$$\frac{\partial u}{\partial t} + C(u) = -\frac{1}{\rho} \frac{\partial p}{\partial x} + V_1(u) + V_2(u) + \frac{1}{Fr^2} g_x - \frac{\sigma_I \kappa}{\rho We} \frac{\partial H}{\partial x}. \quad (20)$$

where

$$C(u) = \frac{\partial(u^2)}{\partial x} + \frac{\partial(uv)}{\partial y} + \frac{\partial(uw)}{\partial z}, \quad (21)$$

$$V_1(u) = \frac{\mu}{\rho Re} \left( \frac{\partial^2 u}{\partial x^2} + \frac{\partial^2 u}{\partial y^2} + \frac{\partial^2 u}{\partial z^2} \right), \quad (22)$$

$$V_2(u) = \frac{1}{\rho Re} \left[ 2 \frac{\partial \mu}{\partial x} \frac{\partial u}{\partial x} + \frac{\partial \mu}{\partial y} \left( \frac{\partial v}{\partial x} + \frac{\partial u}{\partial y} \right) + \frac{\partial \mu}{\partial z} \left( \frac{\partial w}{\partial x} + \frac{\partial u}{\partial z} \right) \right], \quad (23)$$

are the convective ( $C$ ) and viscous ( $V_1, V_2$ ) terms of (19). Eq. (20) is discretized by finite differences at the point  $(i + \frac{1}{2}, j, k)$  of the cell as follows. The time derivative

is discretized by the first order forward difference:

$$\frac{\partial u}{\partial t} \Big|_{i+\frac{1}{2},j,k} = \frac{u_{i+\frac{1}{2},j,k}^{n+1} - u_{i+\frac{1}{2},j,k}^n}{\Delta t}. \quad (24)$$

All the other terms of (20) are discretized at the time level  $n$ , ie, the discretization is considered to be explicit. Thus, in the following equations, the index  $n$  is omitted to simplify the notation.

The pressure gradient is discretized by central differences resulting in

$$\frac{1}{\rho} \frac{\partial p}{\partial x} \Big|_{i+\frac{1}{2},j,k} = \frac{1}{\rho_{i+\frac{1}{2},j,k}} \frac{p_{i+1,j,k} - p_{i,j,k}}{\Delta x}. \quad (25)$$

Notice that it is necessary to evaluate  $\rho$  at the face of the cell ( $\rho_{i+\frac{1}{2},j,k}$ ), and we compute an approximation by averaging the known neighboring values

$$\rho_{i+\frac{1}{2},j,k} = \frac{\rho_{i+1,j,k} + \rho_{i,j,k}}{2}, \quad (26)$$

where  $\rho_{i+1,j,k}$  and  $\rho_{i,j,k}$  are located at the center of the cells sharing the face  $(i + \frac{1}{2}, j, k)$ . Thus

$$\frac{1}{\rho} \frac{\partial p}{\partial x} \Big|_{i+\frac{1}{2},j,k} = \frac{2(p_{i+1,j,k} - p_{i,j,k})}{\Delta x (\rho_{i+1,j,k} + \rho_{i,j,k})}. \quad (27)$$

The viscous term  $V_1(u)$  then becomes

$$\begin{aligned} V_1(u) \Big|_{i+\frac{1}{2},j,k} &= \frac{\mu_{i+\frac{1}{2},j,k}}{\rho_{i+\frac{1}{2},j,k} Re} \left[ \frac{u_{i-\frac{1}{2},j,k} - 2u_{i+\frac{1}{2},j,k} + u_{i+\frac{3}{2},j,k}}{\Delta x^2} \right. \\ &+ \frac{u_{i+\frac{1}{2},j-1,k} - 2u_{i+\frac{1}{2},j,k} + u_{i+\frac{1}{2},j+1,k}}{\Delta y^2} \\ &\left. + \frac{u_{i+\frac{1}{2},j,k-1} - 2u_{i+\frac{1}{2},j,k} + u_{i+\frac{1}{2},j,k+1}}{\Delta z^2} \right], \end{aligned} \quad (28)$$

where  $\rho_{i+\frac{1}{2},j,k}$  is approximated by (26). To compute the viscosity, we use the *harmonic mean*

$$\mu_{i+\frac{1}{2},j,k} = 2 \left( \frac{1}{\mu_{i+1,j,k}} + \frac{1}{\mu_{i,j,k}} \right)^{-1}; \quad (29)$$

this is more accurate than simple averaging [29]. Thus, using (29), (28) becomes

$$\begin{aligned} V_1(u) \Big|_{i+\frac{1}{2},j,k} &= \frac{4}{Re \left( \frac{1}{\mu_{i+1,j,k}} + \frac{1}{\mu_{i,j,k}} \right) (\rho_{i+1,j,k} + \rho_{i,j,k})} \cdot \\ &\left[ \frac{u_{i-\frac{1}{2},j,k} - 2u_{i+\frac{1}{2},j,k} + u_{i+\frac{3}{2},j,k}}{\Delta x^2} + \frac{u_{i+\frac{1}{2},j-1,k} - 2u_{i+\frac{1}{2},j,k} + u_{i+\frac{1}{2},j+1,k}}{\Delta y^2} + \right. \end{aligned}$$

$$\frac{u_{i+\frac{1}{2},j,k-1} - 2u_{i+\frac{1}{2},j,k} + u_{i+\frac{1}{2},j,k+1}}{\Delta z^2} \Big]. \quad (30)$$

To discretize the viscous term  $V_2(u)$ , consider the derivatives at the point  $(i + \frac{1}{2}, j, k)$  of the cell:

$$\begin{aligned} \frac{\partial \mu}{\partial x} \Big|_{i+\frac{1}{2},j,k} &= \frac{\mu_{i+1,j,k} - \mu_{i,j,k}}{\Delta x}, & \frac{\partial \mu}{\partial y} \Big|_{i+\frac{1}{2},j,k} &= \frac{\mu_{i+\frac{1}{2},j+\frac{1}{2},k} - \mu_{i+\frac{1}{2},j-\frac{1}{2},k}}{\Delta y}, \\ \frac{\partial \mu}{\partial z} \Big|_{i+\frac{1}{2},j,k} &= \frac{\mu_{i+\frac{1}{2},j,k+\frac{1}{2}} - \mu_{i+\frac{1}{2},j,k-\frac{1}{2}}}{\Delta z}, & \frac{\partial u}{\partial x} \Big|_{i+\frac{1}{2},j,k} &= \frac{u_{i+1,j,k} - u_{i,j,k}}{\Delta x}, \\ \frac{\partial u}{\partial y} \Big|_{i+\frac{1}{2},j,k} &= \frac{u_{i+\frac{1}{2},j+\frac{1}{2},k} - u_{i+\frac{1}{2},j-\frac{1}{2},k}}{\Delta y}, & \frac{\partial u}{\partial z} \Big|_{i+\frac{1}{2},j,k} &= \frac{u_{i+\frac{1}{2},j,k+\frac{1}{2}} - u_{i+\frac{1}{2},j,k-\frac{1}{2}}}{\Delta z}, \\ \frac{\partial v}{\partial x} \Big|_{i+\frac{1}{2},j,k} &= \frac{v_{i+1,j,k} - v_{i,j,k}}{\Delta x}, & \frac{\partial w}{\partial x} \Big|_{i+\frac{1}{2},j,k} &= \frac{w_{i+1,j,k} - w_{i,j,k}}{\Delta x}. \end{aligned}$$

The unknown velocities in these expressions are calculated by averages of the neighboring known velocities. The values of viscosity on the edges of the cell are computed by an analogous operation to (29), as follows

$$\begin{aligned} \mu_{i+\frac{1}{2},j+\frac{1}{2},k} &= 4 \left( \frac{1}{\mu_{i,j,k}} + \frac{1}{\mu_{i+1,j,k}} + \frac{1}{\mu_{i,j+1,k}} + \frac{1}{\mu_{i+1,j+1,k}} \right)^{-1}, \\ \mu_{i+\frac{1}{2},j-\frac{1}{2},k} &= 4 \left( \frac{1}{\mu_{i,j,k}} + \frac{1}{\mu_{i+1,j,k}} + \frac{1}{\mu_{i,j-1,k}} + \frac{1}{\mu_{i+1,j-1,k}} \right)^{-1}, \\ \mu_{i+\frac{1}{2},j,k+\frac{1}{2}} &= 4 \left( \frac{1}{\mu_{i,j,k}} + \frac{1}{\mu_{i+1,j,k}} + \frac{1}{\mu_{i,j,k+1}} + \frac{1}{\mu_{i+1,j,k+1}} \right)^{-1}, \\ \mu_{i+\frac{1}{2},j,k-\frac{1}{2}} &= 4 \left( \frac{1}{\mu_{i,j,k}} + \frac{1}{\mu_{i+1,j,k}} + \frac{1}{\mu_{i,j,k-1}} + \frac{1}{\mu_{i+1,j,k-1}} \right)^{-1}. \end{aligned}$$

Finally, the discretization of  $V_2(u)$  becomes

$$\begin{aligned} V_2(u) \Big|_{i+\frac{1}{2},j,k} &= \frac{1}{Re(\rho_{i+1,j,k} + \rho_{i,j,k})} \left\{ \frac{(\mu_{i+1,j,k} - \mu_{i,j,k})(u_{i+\frac{3}{2},j,k} - u_{i-\frac{1}{2},j,k})}{\Delta x^2} + \right. \\ &\quad \frac{4}{\Delta y} \left[ \left( \frac{1}{\mu_{i,j,k}} + \frac{1}{\mu_{i+1,j,k}} + \frac{1}{\mu_{i,j+1,k}} + \frac{1}{\mu_{i+1,j+1,k}} \right)^{-1} - \left( \frac{1}{\mu_{i,j,k}} + \frac{1}{\mu_{i+1,j,k}} + \frac{1}{\mu_{i,j-1,k}} + \right. \right. \\ &\quad \left. \left. \frac{1}{\mu_{i+1,j-1,k}} \right)^{-1} \right] \cdot \left( \frac{v_{i+1,j+\frac{1}{2},k} + v_{i+1,j-\frac{1}{2},k} - v_{i,j+\frac{1}{2},k} - v_{i,j-\frac{1}{2},k}}{2\Delta x} + \frac{u_{i+\frac{1}{2},j+1,k} - u_{i+\frac{1}{2},j-1,k}}{2\Delta y} \right) + \\ &\quad \frac{4}{\Delta z} \left[ \left( \frac{1}{\mu_{i,j,k}} + \frac{1}{\mu_{i+1,j,k}} + \frac{1}{\mu_{i,j,k+1}} + \frac{1}{\mu_{i+1,j,k+1}} \right)^{-1} - \left( \frac{1}{\mu_{i,j,k}} + \frac{1}{\mu_{i+1,j,k}} + \frac{1}{\mu_{i,j,k-1}} + \right. \right. \\ &\quad \left. \left. \frac{1}{\mu_{i+1,j,k-1}} \right)^{-1} \right] \cdot \left( \frac{w_{i+1,j,k+\frac{1}{2}} + w_{i+1,j,k-\frac{1}{2}} - w_{i,j,k+\frac{1}{2}} - w_{i,j,k-\frac{1}{2}}}{2\Delta x} + \frac{u_{i+\frac{1}{2},j,k+1} - u_{i+\frac{1}{2},j,k-1}}{2\Delta z} \right) \Big\}. \end{aligned}$$

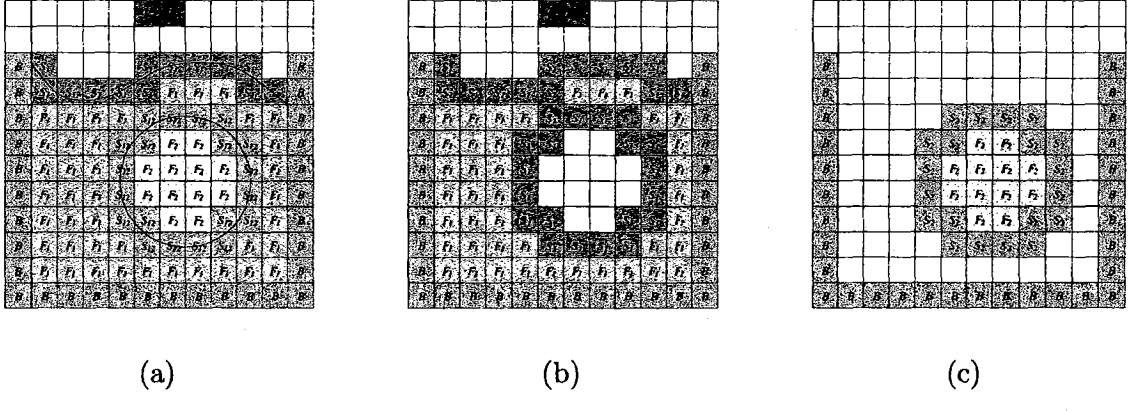


Fig. 2. Multi-fluid cell flagging example: (a) Classification for fluids 1 and 2; (b) Classification only for fluid 1; (c) Classification only for fluid 2.

The discretization of the momentum equations in the  $y$  and  $z$  directions is obtained in a similar manner. The nonlinear terms in the momentum equation are discretized using the high order upwind scheme VONOS, omitted here for brevity. Full details may be found in Ferreira et al. [9]. This scheme is accurate and stable for simulations where the Reynolds number is high.

Using the tracking particles, the free surface and interfaces are approximated by a piecewise linear surface and computationally represented by the “half-edge” data structure [14].

The flow properties are evaluated in a three-dimensional uniform grid, in which every cell, at each time step, is classified according to its position relative to the fluids and the rigid boundaries. Cells with more than half of their volume in a container are classified as BOUNDARY (B) cells; the same criteria is used for the INFLOW (I) cells. Any cell completely inside the fluid is classified as a FULL (F) cell, those completely outside the fluid are EMPTY (E) cells and those on the free surface are SURFACE (S) cells. This criteria is applied to each fluid in the simulation, and the interface cells are identified as the cells that are SURFACE (S) for more than one fluid at the same time. Figure 2 shows an example of cell flagging in a two-dimensional case, with a classification for each fluid.

In order to apply the free surface boundary conditions (17) in each **S** cell, approximations for the surface normals were needed. These have been obtained [28] according to the classification of the neighboring cells. For example:  $\mathbf{n}_c = (\pm 1, 0, 0)$ ,  $\mathbf{n}_c = (0, \pm 1, 0)$  or  $\mathbf{n}_c = (0, 0, \pm 1)$  if only one neighbor is an **E** cell;  $\mathbf{n}_c = (\pm \frac{\sqrt{2}}{2}, \pm \frac{\sqrt{2}}{2}, 0)$ ,

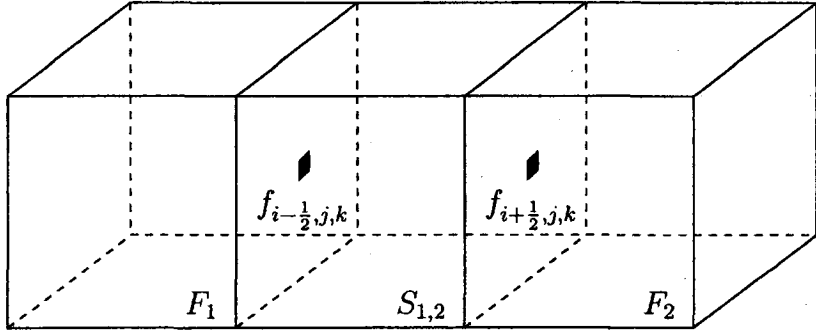


Fig. 3. Interface cell between fluids 1 and 2, with full cells in the opposite faces.

$\mathbf{n}_c = (\pm \frac{\sqrt{2}}{2}, 0, \pm \frac{\sqrt{2}}{2})$  or  $\mathbf{n}_c = (0, \pm \frac{\sqrt{2}}{2}, \pm \frac{\sqrt{2}}{2})$  if there are two neighboring  $\mathbf{E}$  cells, and;  $\mathbf{n}_c = (\pm \frac{\sqrt{3}}{3}, \pm \frac{\sqrt{3}}{3}, \pm \frac{\sqrt{3}}{3})$  if there are three neighboring  $\mathbf{E}$  cells in the  $x$ ,  $y$  and  $z$  directions. Note the notation  $\mathbf{n}_c$  here means the normal at the center of the  $\mathbf{S}$  cell being considered. In order to implement the surface tension effects it is also necessary to estimate the surface curvature at the center of each surface cell, and to take into account sub-cell surface tension effects. In the following sections the methodology employed in the implementation of the surface tension effects is described. This methodology results in a better estimate of the surface normal which is then used in the computation of the capillary pressure.

### 3.1 Interfacial tension effects

To implement the interfacial tension effects into the momentum equation, it is necessary to determine the resulting forces that need to be applied in the discretized domain.

If the mesh is chosen to be sufficiently fine, then the interface can be approximated by the cells containing the front. This approach results in an interface that is at least one cell thick (in most points on the surface the interface will be only one cell thick). So, we have to determine the interfacial tension forces in those cells by a discretized form of

$$\mathbf{f} = -\frac{\sigma_I \kappa}{\rho We} \nabla H,$$

where  $H$  is a Heaviside function that is 1 inside the particular fluid under consideration and 0 outside.

It is convenient to define one Heaviside function  $H_\lambda$  for each fluid  $\lambda$  in the discretized domain taking into account the region defined by the interfacial cells.

Thus,

$$H_\lambda(x, y, z) = \begin{cases} 1, & \text{if } (x, y, z) \text{ is inside a FULL cell or is} \\ & \text{inside an INTERFACE cell of the fluid } \lambda, \\ 0, & \text{otherwise.} \end{cases} \quad (31)$$

such that, the force to be applied in each cell is given by

$$\mathbf{f} = -\frac{\sigma_I}{\rho We} \frac{1}{n} \sum_{\lambda=1}^n \kappa_\lambda \nabla H_\lambda, \quad (32)$$

where  $n$  is the number of fluids involved. Each fluid supplies a different curvature and Heaviside function. For each fluid  $\lambda$  the force is applied at each face of the interfacial cell, which is in contact with an empty cell.

For example, to calculate the force contribution in a single face  $(i - \frac{1}{2}, j, k)$ , as shown in figure 3, we have two Heaviside functions to be discretized,  $H_1$  and  $H_2$ .

$$\begin{aligned} \frac{\partial H_1}{\partial x} \Big|_{i-\frac{1}{2},j,k} &= \frac{H_1(i\Delta x, j\Delta y, k\Delta z) - H_1((i-1)\Delta x, j\Delta y, k\Delta z)}{\Delta x} = 0 \\ \frac{\partial H_2}{\partial x} \Big|_{i-\frac{1}{2},j,k} &= \frac{H_2(i\Delta x, j\Delta y, k\Delta z) - H_2((i-1)\Delta x, j\Delta y, k\Delta z)}{\Delta x} = \frac{1}{\Delta x}, \end{aligned}$$

and then, the resulting force to be applied to face  $(i - \frac{1}{2}, j, k)$  is given by

$$\begin{aligned} f_{i-\frac{1}{2},j,k} &= \frac{-\sigma_I}{\rho_{i-\frac{1}{2},j,k} We} \frac{1}{2} \left( \kappa_1 \frac{\partial H_1}{\partial x} \Big|_{i-\frac{1}{2},j,k} + \kappa_2 \frac{\partial H_2}{\partial x} \Big|_{i-\frac{1}{2},j,k} \right) \\ &= \frac{-\sigma_I \kappa_2}{2\Delta x \rho_{i-\frac{1}{2},j,k} We}. \end{aligned}$$

The other cases are obtained following this procedure. The gradient of the Heaviside functions gives the correct direction of action of the applied forces in any configuration.

#### 4 Curvature calculation

Surface and interfacial tension effects are incorporated using an approach very similar to the one described in [4] for the two-dimensional case. The computation

of the surface and interfacial tension is performed at two levels: first at the sub-grid level, where small undulations in the fronts (free surface and interfaces) are eliminated, and second at cell level, where the curvature at each surface or interface cell is approximated. This approximation will be used in the implementation of the pressure boundary condition at the free surface and in the calculation of the interfacial forces described above.

The curvature is approximated by the surface that best fits the points in that cell and its neighbors. The results presented in [22] suggest the use of an approximation by the paraboloid

$$\pi(x, y) = ax^2 + bxy + cy^2 + dx + ey + f. \quad (33)$$

In this approximation, we first need to determine the normal vector at the cell center. We can summarize the method of curvature approximation by the following steps:

- (1) Given a surface or interface cell, consider all points that lie inside a sphere  $S_\delta$  with its center at the cell center with a given radius  $\delta$ .
- (2) Fit a plane to these points, and compute its normal vector;
- (3) Take a new coordinate system normal to the surface, using the previous computed normal vector;
- (4) Consider a new sphere centered at the cell center,  $S_\varepsilon$  with a chosen radius  $\varepsilon$ , and then map the points in this sphere to the new coordinate system;
- (5) Fit the surface given by (33) to the mapped points, using the new coordinate system;
- (6) Compute the total curvature of the fitted surface using

$$\kappa = \frac{\frac{\partial^2 \pi}{\partial \xi^2}}{\left[1 + \left(\frac{\partial \pi}{\partial \xi}\right)^2\right]^{\frac{3}{2}}} + \frac{\frac{\partial^2 \pi}{\partial \eta^2}}{\left[1 + \left(\frac{\partial \pi}{\partial \eta}\right)^2\right]^{\frac{3}{2}}} \quad (34)$$

where  $\pi$  is the fitted surface satisfying (33), and  $(\xi, \eta, \zeta)$  are the coordinates of the new coordinate system. Note the  $\zeta$ -axis is parallel to the normal vector.

In this method, the quality of the approximations is directly related to the chosen radii  $\delta$  and  $\varepsilon$ . Typically  $\delta$  is chosen to be of the order of the cell size and  $\varepsilon$  1.5 times larger. For more detailed discussion of the influence of these constants see [22], where the optimum choice for these numbers is discussed.

How the normal vector and the curvature approximations are made will be described in detail in the next sub-sections.

#### 4.1 Normal vector approximation

The region  $S_\delta$  associated with each cell  $\mathbf{S}$  will include a number of points. Let us call that number  $m$ ; so  $m = m(\delta)$ . Let  $\mathbf{x}_i = (x_i, y_i, z_i)$ ,  $i = 1, \dots, m_\delta$  be the number of points inside  $S_\delta$  and thus the number of points in cell  $\mathbf{S}$  and its surrounding neighbors. The equation of the plane will be either of  $z = f(x, y)$ ,  $y = f(x, z)$  or  $x = f(y, z)$ , according to the maximum absolute value of cell normal vector components. For example, if  $|\langle \mathbf{n}_c, (0, 0, 1) \rangle| > |\langle \mathbf{n}_c, (1, 0, 0) \rangle|$  and  $|\langle \mathbf{n}_c, (0, 0, 1) \rangle| > |\langle \mathbf{n}_c, (0, 1, 0) \rangle|$ , where  $\langle \cdot, \cdot \rangle$  denotes the inner product, the equation of the plane is given by  $z = f(x, y) = ax + by + c$ , and we need to determine the coefficients  $a$ ,  $b$  and  $c$ , such that the plane  $z = ax + by + c$  approximates the given points. The least squares approximation can be obtained by solving the normal equations

$$\begin{pmatrix} \langle \mathbf{a}, \mathbf{a} \rangle & \langle \mathbf{a}, \mathbf{b} \rangle & \langle \mathbf{a}, \mathbf{c} \rangle \\ \langle \mathbf{b}, \mathbf{a} \rangle & \langle \mathbf{b}, \mathbf{b} \rangle & \langle \mathbf{b}, \mathbf{c} \rangle \\ \langle \mathbf{c}, \mathbf{a} \rangle & \langle \mathbf{c}, \mathbf{b} \rangle & \langle \mathbf{c}, \mathbf{c} \rangle \end{pmatrix} \begin{pmatrix} a \\ b \\ c \end{pmatrix} = \begin{pmatrix} \langle \mathbf{z}, \mathbf{a} \rangle \\ \langle \mathbf{z}, \mathbf{b} \rangle \\ \langle \mathbf{z}, \mathbf{c} \rangle \end{pmatrix} \quad (35)$$

where  $\mathbf{a} = (x_1, \dots, x_m)^T$ ,  $\mathbf{b} = (y_1, \dots, y_m)^T$ ,  $\mathbf{c} = (1, \dots, 1)^T$  and  $\mathbf{z} = (z_1, \dots, z_m)^T$ , where by  $m$  we mean  $m_\delta$ . In this case, the normal vector to the plane  $z = ax + by + c$  is given by

$$\mathbf{n}_s = \frac{(a, b, -1)}{\|(a, b, -1)\|}. \quad (36)$$

For the other cases, this process is analogous. This procedure determines  $\mathbf{n}_s$ , but the sign may be incorrect. The correct sign can be determined by comparing  $\mathbf{n}_s$  with the normal at the cell center  $\mathbf{n}_c$ , previously obtained (see section 3). If  $\langle \mathbf{n}_c, \mathbf{n}_s \rangle > 0$  the sign is correct; otherwise the sign must be reversed.

#### 4.2 Quadratic fitting

Now let  $\mathbf{x}_i = (x_i, y_i, z_i)$ ,  $i = 0, \dots, m_\epsilon$  be the points lying in  $S_\epsilon$ . With the normal vector  $\mathbf{n}_s$  given by the plane fitting technique of section 4.1, we choose another

two tangent vectors at the surface such that they, together with the normal vector, form an orthonormal basis. First, we choose two of the three canonical vectors  $\mathbf{e}_1 = (1, 0, 0)$ ,  $\mathbf{e}_2 = (0, 1, 0)$  and  $\mathbf{e}_3 = (0, 0, 1)$  such that their projections on the direction of  $\mathbf{n}_s$  vector are the smallest. Secondly, we apply the Gramm Schmidt method to obtain the orthonormal basis. Thus, we have a new coordinate system and the points  $\mathbf{x}_i$  can be written using this new coordinate system as  $\xi_i = (\xi_i, \eta_i, \zeta_i)$ . Then, we can fit a paraboloid given by  $\hat{\pi}(\xi, \eta) = a\xi^2 + b\xi\eta + c\eta^2 + d\xi + e\eta + f$ . The parameters  $a, b, c, d, e$ , and  $f$  are obtained by solving

$$\begin{pmatrix} \langle \mathbf{a}, \mathbf{a} \rangle & \langle \mathbf{a}, \mathbf{b} \rangle & \langle \mathbf{a}, \mathbf{c} \rangle & \langle \mathbf{a}, \mathbf{d} \rangle & \langle \mathbf{a}, \mathbf{e} \rangle & \langle \mathbf{a}, \mathbf{f} \rangle \\ \langle \mathbf{b}, \mathbf{a} \rangle & \langle \mathbf{b}, \mathbf{b} \rangle & \langle \mathbf{b}, \mathbf{c} \rangle & \langle \mathbf{b}, \mathbf{d} \rangle & \langle \mathbf{b}, \mathbf{e} \rangle & \langle \mathbf{b}, \mathbf{f} \rangle \\ \langle \mathbf{c}, \mathbf{a} \rangle & \langle \mathbf{c}, \mathbf{b} \rangle & \langle \mathbf{c}, \mathbf{c} \rangle & \langle \mathbf{c}, \mathbf{d} \rangle & \langle \mathbf{c}, \mathbf{e} \rangle & \langle \mathbf{c}, \mathbf{f} \rangle \\ \langle \mathbf{d}, \mathbf{a} \rangle & \langle \mathbf{d}, \mathbf{b} \rangle & \langle \mathbf{d}, \mathbf{c} \rangle & \langle \mathbf{d}, \mathbf{d} \rangle & \langle \mathbf{d}, \mathbf{e} \rangle & \langle \mathbf{d}, \mathbf{f} \rangle \\ \langle \mathbf{e}, \mathbf{a} \rangle & \langle \mathbf{e}, \mathbf{b} \rangle & \langle \mathbf{e}, \mathbf{c} \rangle & \langle \mathbf{e}, \mathbf{d} \rangle & \langle \mathbf{e}, \mathbf{e} \rangle & \langle \mathbf{e}, \mathbf{f} \rangle \\ \langle \mathbf{f}, \mathbf{a} \rangle & \langle \mathbf{f}, \mathbf{b} \rangle & \langle \mathbf{f}, \mathbf{c} \rangle & \langle \mathbf{f}, \mathbf{d} \rangle & \langle \mathbf{f}, \mathbf{e} \rangle & \langle \mathbf{f}, \mathbf{f} \rangle \end{pmatrix} \begin{pmatrix} a \\ b \\ c \\ d \\ e \\ f \end{pmatrix} = \begin{pmatrix} \langle \mathbf{z}, \mathbf{a} \rangle \\ \langle \mathbf{z}, \mathbf{b} \rangle \\ \langle \mathbf{z}, \mathbf{c} \rangle \\ \langle \mathbf{z}, \mathbf{d} \rangle \\ \langle \mathbf{z}, \mathbf{e} \rangle \\ \langle \mathbf{z}, \mathbf{f} \rangle \end{pmatrix} \quad (37)$$

where  $\mathbf{a} = (\xi_1^2, \dots, \xi_m^2)^T$ ,  $\mathbf{b} = (\xi_1\eta_1, \dots, \xi_m\eta_m)^T$ ,  $\mathbf{c} = (\eta_1^2, \dots, \eta_m^2)^T$ ,  $\mathbf{d} = (\xi_1, \dots, \xi_m)^T$ ,  $\mathbf{e} = (\eta_1, \dots, \eta_m)^T$ ,  $\mathbf{f} = (1, \dots, 1)^T$ , and  $\mathbf{z} = (\zeta_1, \dots, \zeta_m)^T$ , where by  $m$  we mean  $m_\varepsilon$ .

The total curvature is then given by

$$\kappa = -2 \left( \frac{a}{(1 + d^2)^{\frac{3}{2}}} + \frac{c}{(1 + e^2)^{\frac{3}{2}}} \right) . \quad (38)$$

## 5 Undulations removal

In many applications, in particular when the Reynolds number is high (larger than 50), small undulations may appear at the free surface and at the interfaces. This is due to variations in the velocity field from cell to cell and may be amplified in regions where the surface area is shrinking. These undulations are frequently much smaller than a cell size and usually they are not present in real flows. They are physically removed by a combination of surface or interfacial tension and viscous effects. A numerical implementation that acts at cell level, like the method pre-

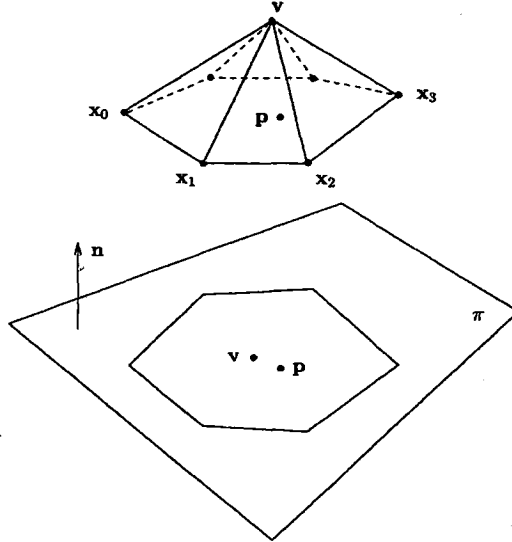


Fig. 4. A typical vertex and its star projected into the plane  $\pi$ .

sented above, cannot take into account these sub-cell undulations and correctly suppress them.

There are several approaches that can be used to suppress these unphysical undulations such as applying a Gaussian filter. However, in fluid flow simulations it is important that the technique applied does not alter the mass of the flow (or the volume in the case of an incompressible fluid).

We developed a filter called TSUR-3D (TSUR: Trapezoidal Sub-grid Undulations Removal) which is based on the TSUR filter presented in [4] for the two-dimensional case. The TSUR-3D is applied to the unstructured grid, represented by a “*half-edge*” data structure [14]. Figure 4 shows a typical vertex  $v$ , and its corresponding star, formed by the set of vertices  $x_i$  which are connected to it with typical edges  $(v, x_i)$  and  $(x_i, x_{i+1})$ , and the typical faces  $(x_i, v, x_{i+1})$ ,  $i = 0, 1, \dots, n$ , where  $x_{n+1}$  is to be interpreted as  $x_0$ .

Since we are interested in local changes in volume, we define a local volume as the volume bounded by the faces  $(x_i, v, x_{i+1})$  and  $(x_i, p, x_{i+1})$ ,  $i = 0, 1, \dots, n$ , where  $p$  is an arbitrary point, as shown in figure 5,

The balance procedure first determines a plane  $\pi$  defined by the normal computed from the average of the normals of the vertices  $x_i$ ,  $i = 0, 1, \dots, n$ . The vertex  $v$  and the vertices  $x_i$ ,  $i = 0, 1, \dots, n$ , are projected onto that plane and  $v$  is centered in that plane, and the correct height of the new vertex in the direction of the normal

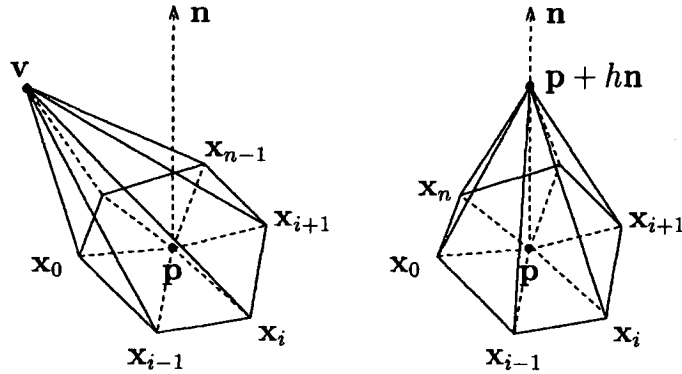


Fig. 5. A vertex with its star, before and after the vertex balance procedure has been applied.

of the plane is chosen so that the local volume is preserved (see figure 4).

This procedure smoothes small undulations and keeps the volume of the fluid unchanged. The steps of the method are explained in the following sections.

### 5.1 Normal vector calculation

Both vertex balance and undulation removal procedures require a normal direction, which is obtained using information from the neighboring vertices  $\mathbf{x}_i$ ,  $i = 0, 1, \dots, n$ . Let  $\mathbf{v}$  be a vertex of the interface, and let  $S(\mathbf{v})$  be the star of  $\mathbf{v}$ . Let  $\mathbf{p}$  be the average of the vertices in  $S(\mathbf{v})$ , given by

$$\mathbf{p} = \frac{1}{n} \sum_{i=0}^n \mathbf{x}_i \quad (39)$$

where  $\mathbf{x}_0, \mathbf{x}_1, \dots, \mathbf{x}_n \in S(\mathbf{v})$ . Thus, we can compute the normal vector by the average of the normal vectors at the faces  $(\mathbf{x}_i, \mathbf{p}, \mathbf{x}_{i+1})$  ( $i = 0, 1, \dots, n$ ), given by

$$\mathbf{n} = \frac{\sum_{i=0}^{n-1} (\mathbf{x}_i - \mathbf{p}) \times (\mathbf{x}_{i+1} - \mathbf{p}) + (\mathbf{x}_n - \mathbf{p}) \times (\mathbf{x}_0 - \mathbf{p})}{\| \sum_{i=0}^{n-1} (\mathbf{x}_i - \mathbf{p}) \times (\mathbf{x}_{i+1} - \mathbf{p}) + (\mathbf{x}_n - \mathbf{p}) \times (\mathbf{x}_0 - \mathbf{p}) \|}. \quad (40)$$

where  $\times$  denotes the vector product. Note this is a weighted average: normals of faces with greater area will be given greater weight. This equation gives a robust normal direction for this method.



## 5.2 Vertex balance procedure

The vertex balance procedure is applied at each vertex of the fluid in order to move it to a new position on a line passing through  $\mathbf{p}$ , given by (39) with the direction  $\mathbf{n}$  given by (40), such that the local volume is preserved. Let  $\pi$  be a plane that contains  $\mathbf{p}$ , with normal vector  $\mathbf{n}$ . If  $\mathbf{p}$  is inside the projection of  $S(\mathbf{v})$  onto  $\pi$ , we compute the new position of  $\mathbf{v}$  by

$$\mathbf{v}_{\text{new}} = \mathbf{p} + h\mathbf{n} \quad (41)$$

where  $h$  is determined such that the local volume is preserved. This is guaranteed if

$$V = hV_1 \quad \text{or} \quad h = \frac{V}{V_1} \quad (42)$$

where  $V$  is the volume of the polyhedron  $(\mathbf{v}, \mathbf{x}_0, \mathbf{x}_1, \dots, \mathbf{x}_n, \mathbf{p})$  and  $V_1$  is the volume of the unitary polyhedron  $(\mathbf{p} + \mathbf{n}, \mathbf{x}_0, \mathbf{x}_1, \dots, \mathbf{x}_n, \mathbf{p})$ . This is because the volume of the polyhedron  $(\mathbf{p} + h\mathbf{n}, \mathbf{x}_0, \mathbf{x}_1, \dots, \mathbf{x}_n, \mathbf{p})$  is equal to  $h$  times the volume of the unitary polyhedron  $(\mathbf{p} + \mathbf{n}, \mathbf{x}_0, \mathbf{x}_1, \dots, \mathbf{x}_n, \mathbf{p})$ .

The volume of a tetrahedron  $(\mathbf{x}_1, \mathbf{x}_2, \mathbf{x}_3, \mathbf{x}_4)$  is given by

$$V = \frac{1}{6} \cdot \det \begin{vmatrix} x_2 - x_1 & x_3 - x_1 & x_4 - x_1 \\ y_2 - y_1 & y_3 - y_1 & y_4 - y_1 \\ z_2 - z_1 & z_3 - z_1 & z_4 - z_1 \end{vmatrix}. \quad (43)$$

Since the volume of any polyhedron may be considered to be the sum of the volumes of several tetrahedra, this can be straightforwardly calculated.

As we can see in figure 5 this procedure does not remove any undulations, but just moves the vertex to a new position, that is better centered in its star, improving the quality of the surface mesh, while preserving local volume. This improves the robustness of the undulation removal procedure presented below.

## 5.3 Undulation removal procedure

The vertex balance procedure is designed to produce a more homogeneous unstructured grid that represents the free surface or interface. However, it cannot remove

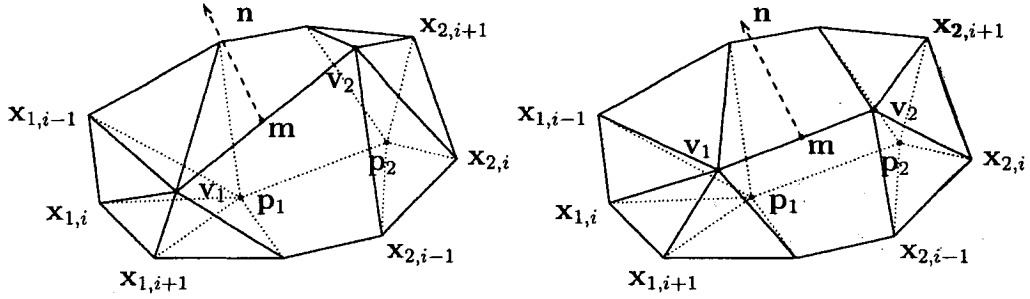


Fig. 6. Undulation removal procedure, showing an edge and its star.

the sub-grid undulations, and a smoothing procedure is required for the effective removal of these undulations.

Let  $e$  be an edge of the surface, and  $v_1, v_2$  its vertices, as shown in figure 6. The smoothing procedure changes the position of  $v_1$  and  $v_2$  simultaneously, such that the local volume is preserved. Let  $n_1$  and  $n_2$  be the normal vectors computed by (40) at the vertices  $v_1$  and  $v_2$ , respectively. We consider a normal vector at the edge  $e$ , given by the average of  $n_1$  and  $n_2$ ,

$$\mathbf{n} = \frac{\mathbf{n}_1 + \mathbf{n}_2}{\|\mathbf{n}_1 + \mathbf{n}_2\|}. \quad (44)$$

Let

$$\mathbf{m} = \frac{1}{2}(\mathbf{v}_1 + \mathbf{v}_2) \quad (45)$$

be the average of the vertices of the edge  $e$ . We determine the heights  $h_1$  and  $h_2$  in the direction of this normal vector by

$$h_1 = \langle \mathbf{v}_1 - \mathbf{m}, \mathbf{n} \rangle \quad \text{and} \quad h_2 = \langle \mathbf{v}_2 - \mathbf{m}, \mathbf{n} \rangle \quad (46)$$

where  $\langle \cdot, \cdot \rangle$  denotes the inner product. Next, we compute the points  $\mathbf{p}_1$  and  $\mathbf{p}_2$  by

$$\mathbf{p}_1 = \mathbf{v}_1 - h_1 \mathbf{n} \quad \text{and} \quad \mathbf{p}_2 = \mathbf{v}_2 - h_2 \mathbf{n}. \quad (47)$$

Thus, we have two polyhedra,  $(\mathbf{v}_1, \mathbf{x}_{10}, \dots, \mathbf{x}_{1n}, \mathbf{p}_1)$  with volume  $V_1$  and  $(\mathbf{v}_2, \mathbf{x}_{20}, \dots, \mathbf{x}_{2m}, \mathbf{p}_2)$  with volume  $V_2$ , where  $\mathbf{x}_{10}, \dots, \mathbf{x}_{1n} \in S(\mathbf{v}_1)$  and  $\mathbf{x}_{20}, \dots, \mathbf{x}_{2m} \in S(\mathbf{v}_2)$  (see figure 6). We have to determine a new height  $h$  in the direction of  $\mathbf{n}$ , such that the local volume is preserved.

We can exploit linearity between the volumes of the polyhedra and the heights and write

$$V_1 + V_2 = V_1(h/h_1) + V_2(h/h_2) \quad (48)$$

or

$$h = \frac{V_1 + V_2}{V_1/h_1 + V_2/h_2}. \quad (49)$$

The new positions of the vertices  $\mathbf{v}_1$  and  $\mathbf{v}_2$  are given by

$$\mathbf{v}_1 = \mathbf{p}_1 + h\mathbf{n} \quad \text{and} \quad \mathbf{v}_2 = \mathbf{p}_2 + h\mathbf{n}. \quad (50)$$

This undulation removal procedure is applied periodically to all the edges of the surface mesh with a period that has to be chosen such that the surface is sufficiently smooth, and the large scale undulations are not strongly affected. The frequency of applications is dependent on the problem, the grid resolution, and the time step.

## 6 Validation and numerical results

A number of tests was performed to validate the code and to assess its robustness and precision. First, we present some numerical results to validate the surface and interfacial tension computation, and to show the improvement of the TSUR-3D filter on the free surfaces or interfaces.

In the following subsections multi-fluid flow calculations are compared with their analytic solutions. In particular we shall consider an oscillatory bubble, a bubble rising in a continuous phase and bubble coalescence. Finally the splashing drop problem (with two phases) will be simulated to illustrate the capability and emphasize the robustness of the code.

### 6.1 Capillary pressure of spherical bubbles

To validate the computation of the interfacial tension and the capillary pressure, the problem of a spherical fluid (or bubble) of one phase is immersed into a fluid of another phase. This is then simulated using different grids. The densities of the fluids are  $\rho_d = 1 \text{ g/cm}^3$  for the bubble and  $\rho_f = 0.5 \text{ g/cm}^3$  for the continuous phase. The interface tension coefficient is  $\sigma = 23.61 \text{ dyn/cm}$ , and the radius of the bubble is  $R = 2 \text{ cm}$ . Figure 7 shows the pressure jump at the interface, at the plane  $y = 3 \text{ cm}$ . In the absence of viscous, gravitational, or external forces, surface or interface tension causes a static liquid bubble to become spherical. The

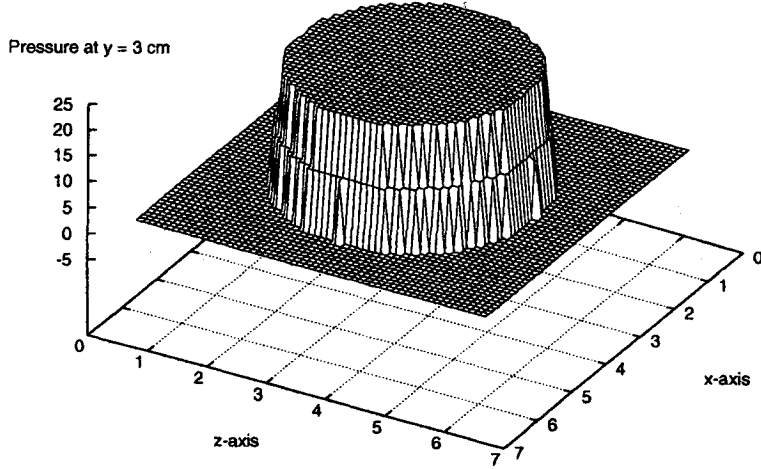


Fig. 7. Capillary pressure of a spherical bubble in a  $60 \times 60 \times 60$  grid, at  $y = 3 \text{ cm}$ .

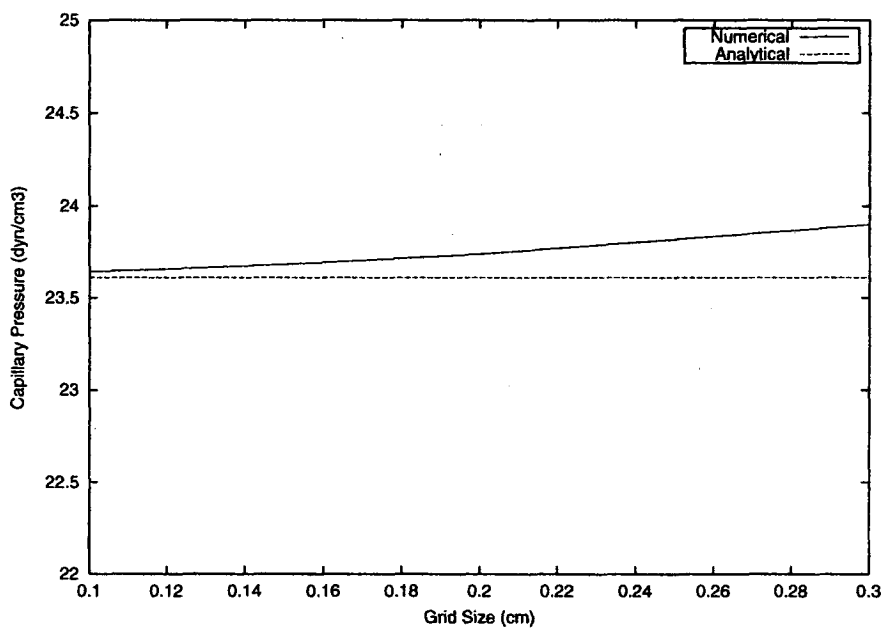
Young-Laplace [3] equation for the capillary pressure is given by

$$\Delta p = \sigma \kappa = \sigma \left( \frac{1}{R_1} + \frac{1}{R_2} \right)$$

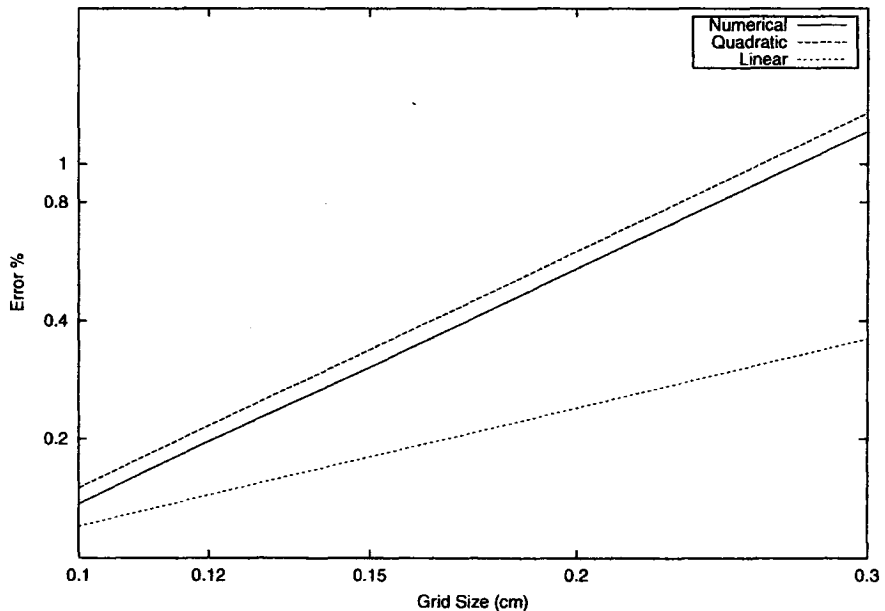
where  $R_1$  and  $R_2$  are the radii of the two perpendicular maximum circles of the sphere. In this case, the analytical value of the pressure jump at the interface is  $\Delta p = 23.61 \text{ dyn/cm}^3$ , deducible directly from the Young-Laplace equation.

Numerical simulations were performed for five different uniform grids, with 20, 30, 40, 50 and 60 cells in each direction. Figure 8 displays the numerical capillary pressure converging to the analytic value given by the Young-Laplace equation (a), and the error as the grid is refined (b).

These numerical results are accurate with an error in the Euclidean norm smaller than 1.2% for the coarsest grid, reduced to about 0.2% when the grid is refined. The convergence of the method for interface tension calculation is quadratic, or order 2, as can be seen in figure 8 (b).



(a)



(b)

Fig. 8. Numerical capillary pressure displaying convergence to the analytical capillary pressure (a) and a log scale graph showing the second order convergence (b).

## 6.2 Sessile drop

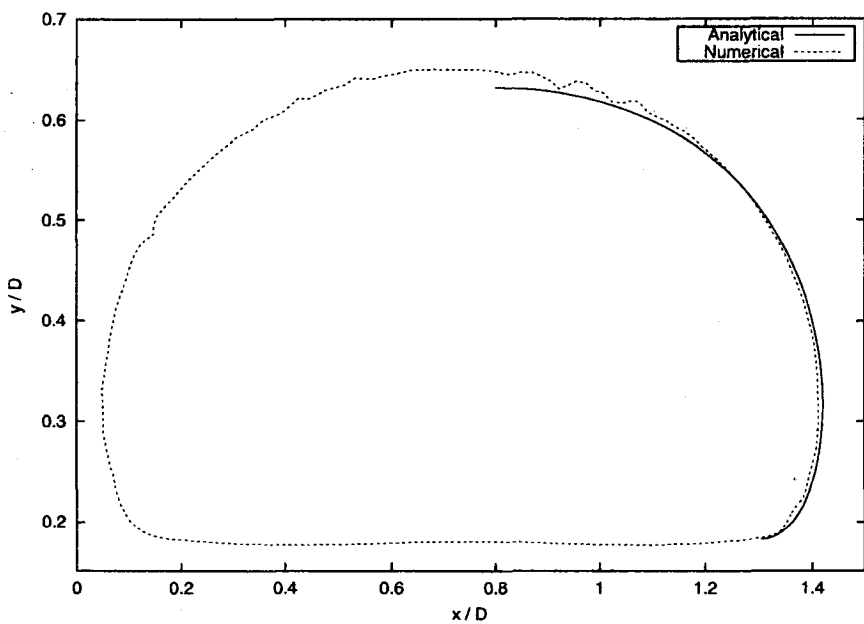
A simulation of a single phase sessile drop was performed to validate the surface tension and curvature calculations. The steady state numerical solutions were obtained from the asymptotic steady state solutions of the transient solution, starting from a spherical drop initially at rest on a plane. Highly accurate solutions were obtained by the numerical integration of the equations for the equilibrium position of an axisymmetric free surface liquid drop. These are, in non-dimensional form, given by

$$\frac{d\theta}{ds} = \text{Bo}(p - z) - \frac{\cos \theta}{r}, \quad \frac{dr}{ds} = -\sin \theta \quad \text{and} \quad \frac{dz}{ds} = \cos \theta, \quad (51)$$

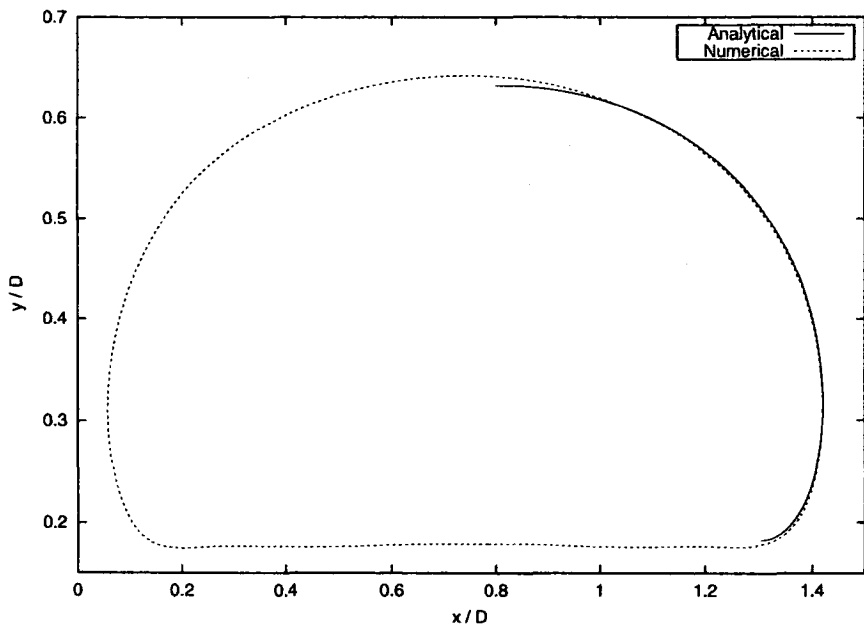
where  $\theta$  is the angle between the surface outward normal and the  $r$  axis,  $s$  is the coordinate along the surface,  $\text{Bo} = \rho g L^2 / \sigma$  is the Bond number, and  $p = \hat{p} / \rho g L$  is a non-dimensional reference pressure, where here  $\hat{p}$  is the dimensional reference pressure.

A fourth-order Runge-Kutta method has been used to integrate (51), using an integration step  $\Delta s = 10^{-4}$ . Hence the solutions can be regarded as being very accurate, aside from a region in the vicinity of the axis  $r = 0$ , where the singularity  $\sin \theta / r$  may degrade the accuracy. To avoid integrating close to the singularity, we start the integration from the point of maximum  $r$  and integrate up to the meniscus, and then down to the contact point. The loss of accuracy of this "exact" solution is therefore restricted to a very small region in the vicinity of the axis, and is therefore, for our purposes, of no concern. A quantitative comparison of the results can be seen in figure 9. Figure 9 (a) shows good agreement between the "exact" and numerical computations of this paper. We would like to emphasize that the above results were obtained using  $28 \times 28 \times 28$  computational cells.

The largest departure from the "exact" solution is observed at the top of the drop in figure 9 (a), where the numerical solution shows some short wavelength (sub-grid) undulations. The occurrence of undulations has been observed to become more pronounced as the Reynolds number is increased, thus requiring the application of a sub-grid filter when simulating flows with higher Reynolds number (above 50). The application of a sub-grid filter improves the results of the method, as can be seen in figure 9 (b).



(a)



(b)

Fig. 9. Comparison between "exact" and numerical solution: without applying the TSUR-3D filter (a), and with the TSUR-3D filter (b).

### 6.3 Oscillation of a bubble

To verify that the transfer between the surface energy and kinetic energy is correctly accounted for, which is important when the flow is dominated by surface tension effects, we validated the method on an ellipsoidal oscillating bubble, for which an analytical solution for the oscillation frequency exists.

This problem consists of simulating an ellipsoidal bubble immersed in a continuous phase without a gravity field. The bubble has a small initial perturbation with respect to its equilibrium spherical form and, driven by the interfacial forces, it tends to oscillate. The non-dimensional parameters chosen for the simulation were  $\sigma = 10$ ,  $\rho_d = 100$  and  $\mu_d = 0.35$  for the bubble and  $\rho_f = 1$  and  $\mu_f = 0.001$  for the surrounding fluid. The bubble's initial diameter was 1 and the initial amplitude of the perturbation corresponds to 2.5% of its radius. The calculations were made in a domain of size  $4R \times 4R \times 4R$ , discretized by a  $40 \times 40 \times 40$  grid. The results obtained were compared with analytic solutions [7,8,32], as can be seen in figure 10. The analytic expression for the frequency oscillation of a bubble in an infinite domain is given by

$$\omega^2 = \frac{24\sigma}{(3\rho_d + 2\rho_f)R^3}.$$

Assuming the viscous effects to be small, the amplitude will decay as

$$a(t) = a_0 e^{-t/\tau},$$

if the effect of the surrounding fluid is neglected, where  $\tau = R/5\nu$  and  $a_0$  and  $\nu$  are the initial amplitude and kinematic viscosity, respectively.

Figure 10 shows a comparison between the numerical result and the analytical curve, given by

$$y(t) = y_0 + a_0 e^{-t/\tau} \cos(\omega t)$$

where  $y_0$  and  $a_0$  are the initial oscillating axis position and the amplitude.

It can be seen that the numerical results are in good agreement with the analytical expression for the bubble diameter. Using the extreme points to estimate the period of oscillation, we found the discrepancy between the numerical and the analytical value for the period is about 12%. This discrepancy can, in part, be attributed to the finite domain used in the numerical simulation, in comparison with the analytical solution which is valid over an infinite domain.

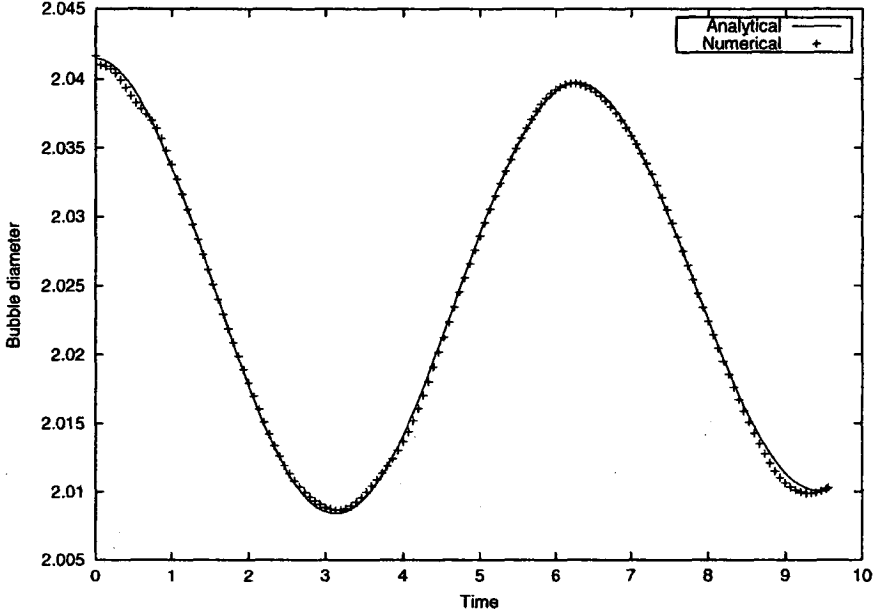


Fig. 10. Oscillation of the bubble diameter as a function of non-dimensional time. It was found that the period was in error by 12%.

#### 6.4 Bubble rising in a continuous phase

Rising bubbles are classical examples that may be used to validate multi-fluid flow simulations. Bubbles with lower density than the surrounding fluid tend to rise, due to the buoyancy effects resulting from the pressure gradient caused by gravity.

In this paper, two numerical results of rising bubbles with low and moderate Reynolds numbers are presented. The results are compared with results published by Esmaeeli & Tryggvason [7,8].

##### 6.4.1 Low Reynolds numbers

The nondimensional parameters, extracted from Esmaeeli & Tryggvason (1998) [7], are given by

$$Eo = 1.0; \quad N = 10^{3/2}; \quad \gamma = 0.05; \quad \lambda = 0.05;$$

where  $Eo = \rho_0 g D^2 / \sigma_0$  is the Eötvös number,  $N = \rho_0^2 D^3 g / \mu_0^2$  is the Galileo or Archimedes number,  $\gamma$  is the density ratio between the bubble and the fluid ( $\rho_b / \rho_f$ ) and  $\lambda$  is the viscosity ratio between the bubble and the fluid ( $\mu_b / \mu_f$ ). These parameters can be obtained by using a 1.9 mm diameter bubble immersed in engine oil, with  $\sigma_I = 0.03 \text{ N/m}$ ,  $\rho_f = 880 \text{ kg/m}^3$  and  $\mu_f = 0.21 \text{ Ns/m}^2$ . The lengths were

nondimensionalized by the diameter  $D = 1.9 \text{ mm}$  and the velocities by  $U = \sqrt{gD}$ .

To compare the results with [7], it is necessary to compute the rising velocity and the centroid position of the bubble at each time step. As the bubble surface is explicitly marked by moving particles, it is more convenient to change the volume integrals into surface integrals using the divergence theorem. Thus, if the bubble volume is given by

$$V_b = \int_{V_b} dV = \frac{1}{3} \oint_{S_b} \mathbf{x} \cdot \mathbf{n} \, dS,$$

then the centroid position is

$$\mathbf{x}_c = \frac{1}{V_b} \int_{V_b} \mathbf{x} \, dV = \frac{1}{2V_b} \oint_{S_b} (\mathbf{x} \cdot \mathbf{x}) \mathbf{n} \, dS,$$

and, using the continuity equation, the rising velocity is given by

$$W_b = \frac{1}{V_b} \int_{V_b} w \, dV = \frac{1}{V_b} \oint_{S_b} (z\mathbf{u}) \cdot \mathbf{n} \, dS.$$

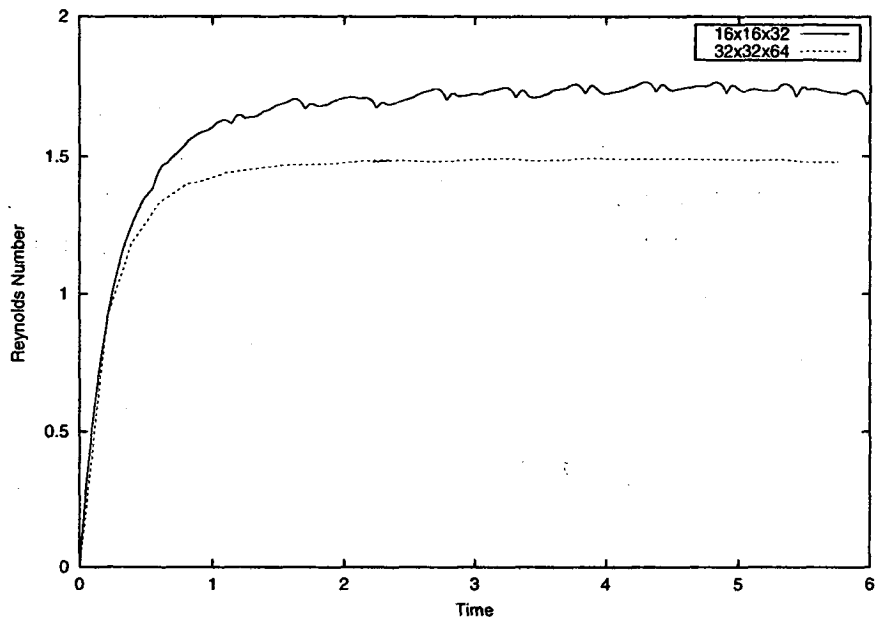
Figure 11 shows the results obtained on grids with  $16 \times 16 \times 32$  and  $32 \times 32 \times 64$  cells. In this figure small oscillations in the rising velocity can be observed. These were eliminated when the grid was refined. The rising velocity oscillates due the pressure gradient in the coarse grid when the bubble moves from cell to cell. At the terminal velocity of the bubble, the Reynolds number obtained (see figure 11 (a) ) is quite close to 1.4. This is the same value obtained by Esmaeeli and Tryggvason [7].

#### 6.4.2 Moderate Reynolds numbers

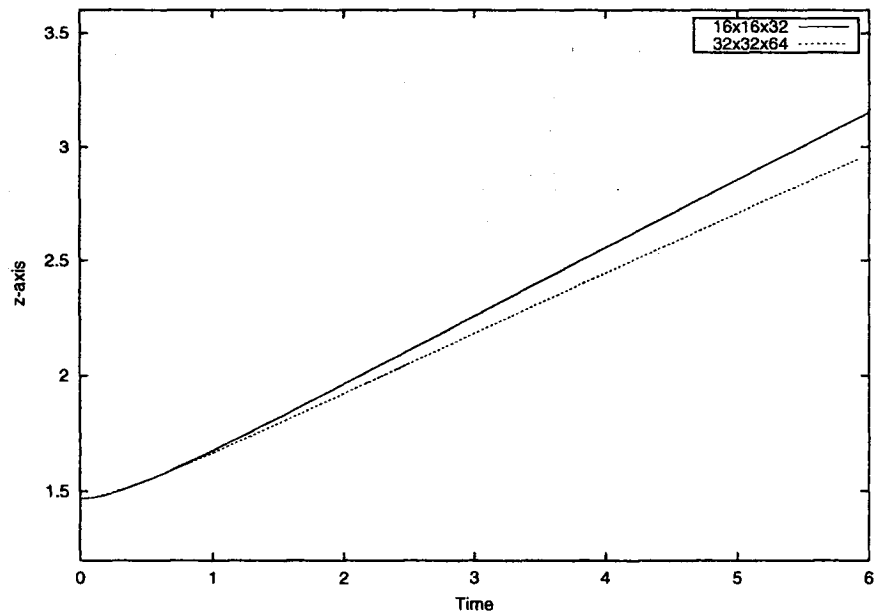
For this simulation, the nondimensional parameters extracted from Esmaeeli and Tryggvason [8], are

$$Eo = 2; \quad N = 894.4; \quad \gamma = 0.1; \quad \lambda = 0.1.$$

These can be obtained from  $D = 2.6 \text{ mm}$  diameter bubble, with  $\mu_f = 0.0125 \text{ Ns/m}^2$ ,  $\rho_f = 880 \text{ kg/m}^3$  for the continuous phase (fluid) and interfacial tension coefficient given by  $\sigma_I = 0.03 \text{ N/m}$ . The lengths were nondimensionalized by the diameter  $D$  and the velocities by  $U = \sqrt{gD}$ .

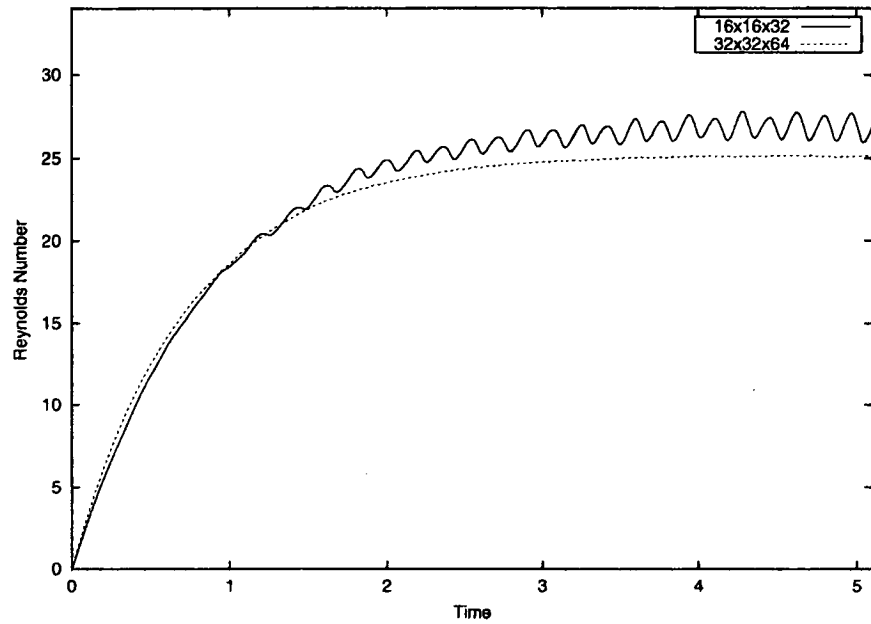


(a)

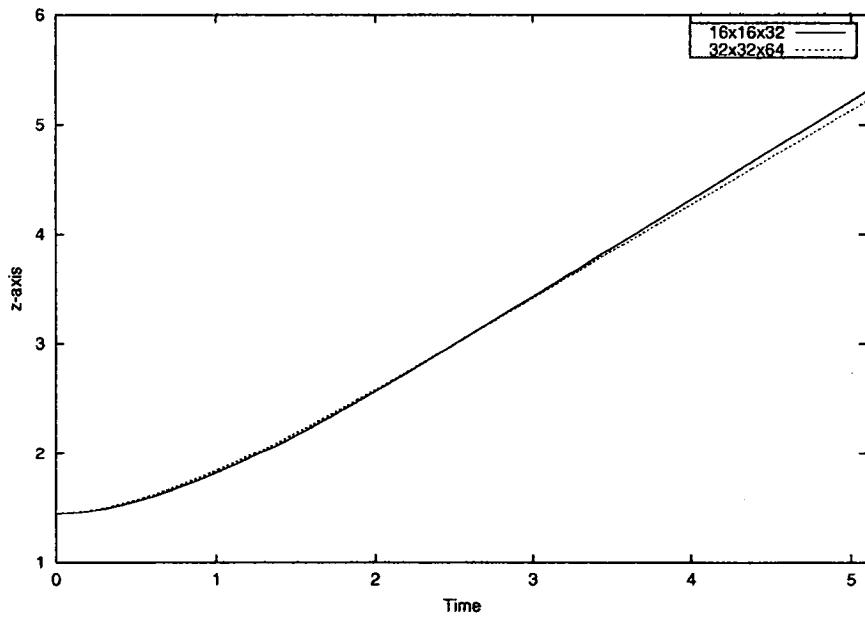


(b)

Fig. 11. Rising Reynolds number (a) and the bubble centroid position (b) plotted against nondimensional time on  $16 \times 16 \times 32$  and  $32 \times 32 \times 64$  grid cells (low Reynolds number case).



(a)



(b)

Fig. 12. Rising Reynolds number (a) and the bubble centroid position (b) plotted against nondimensional time on  $16 \times 16 \times 32$  and  $32 \times 32 \times 64$  grid cells (moderate Reynolds number case).

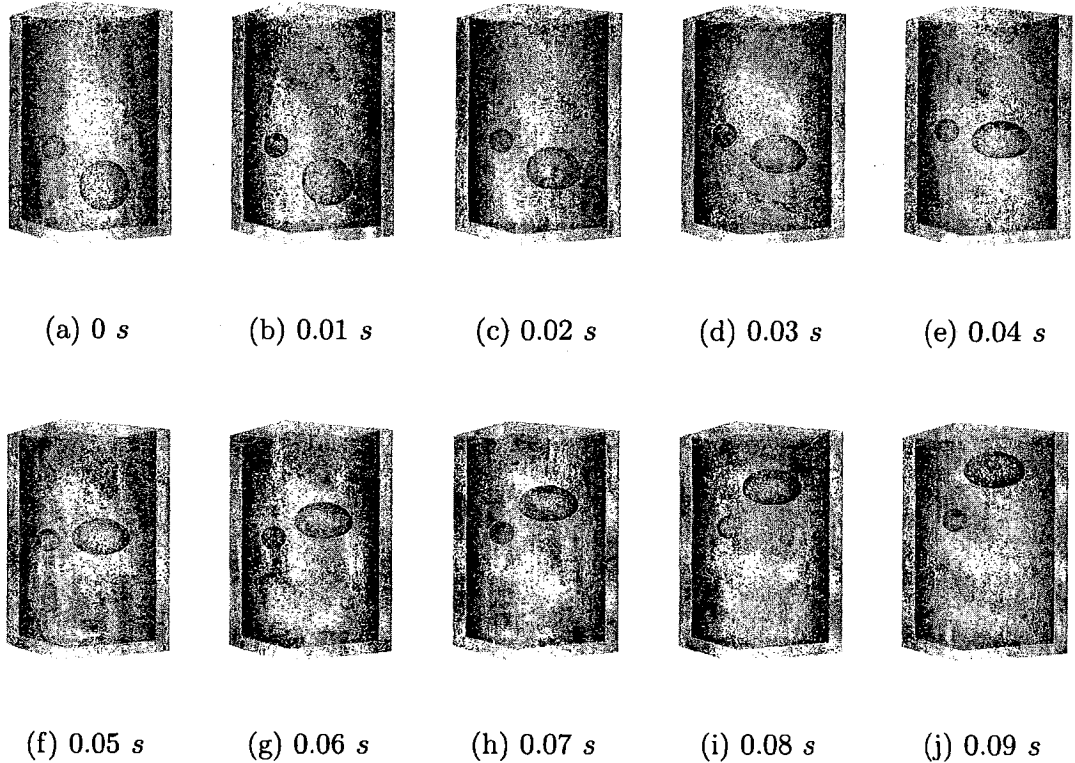


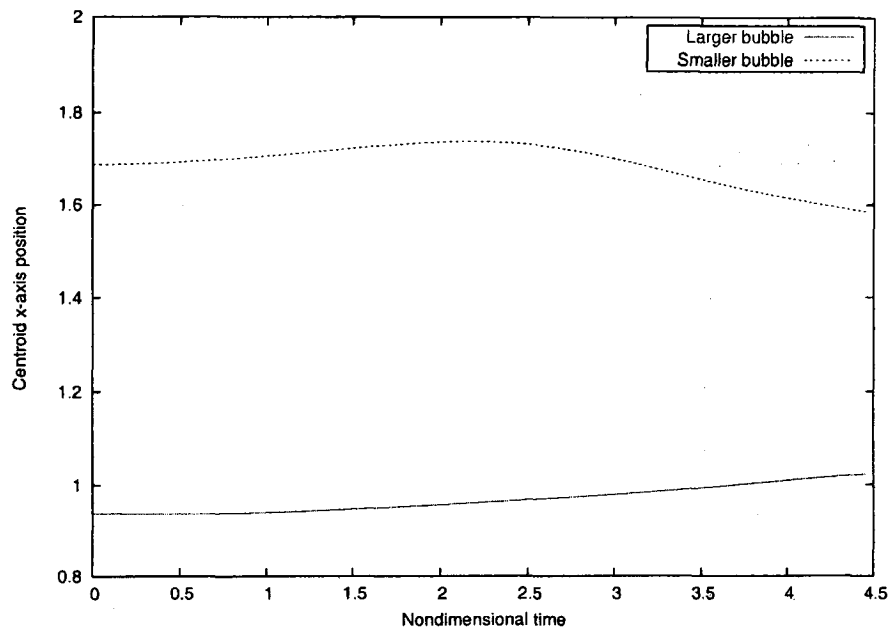
Fig. 13. Two bubbles rising with different densities and viscosities.

As in the low Reynolds number case, the numerical results were compared with those obtained by Esmaeeli and Tryggvason [8], by calculating the rising velocity and centroid position of the bubble. The graphs of these quantities can be seen in figure 12. As in the previous simulation, the results show small oscillations in the rising velocity that vanish when the grid is refined.

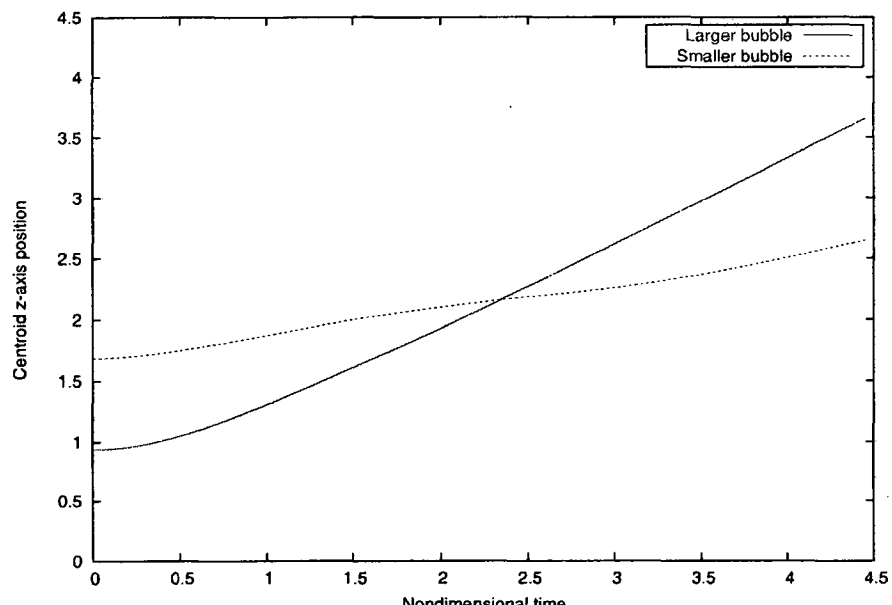
The results obtained by Esmaeeli and Tryggvason [8] show that the fully developed Reynolds number is about 20.5, while the result obtained here is  $Re \approx 25$ . This discrepancy is due to some differences in the boundary conditions between the two models. However, the results obtained are qualitatively similar.

### 6.5 Rising of two different bubbles

This example shows the simulation of the three-fluid flow of two bubbles with different densities, viscosities and diameters, rising in a third phase with a greater density.



(a)



(b)

Fig. 14. Rising of two different bubbles: (a) coordinate  $x$  and (b) coordinate  $z$  of the bubbles centroid position plotted against nondimensional time.

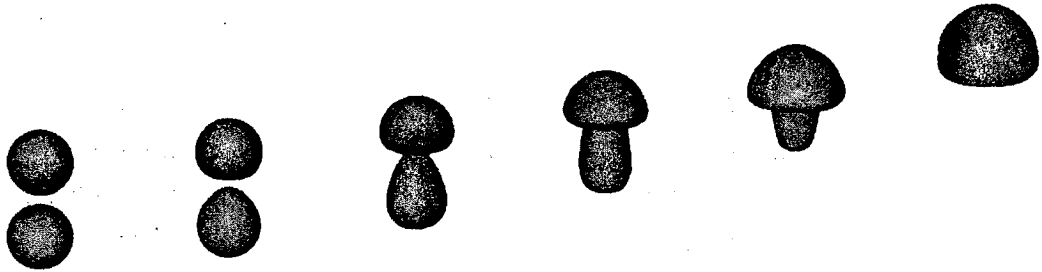


Fig. 15. Transient solution of the bubble coalescence in a continuous phase, with in-line bubbles, for  $t = 0.0$  s,  $t = 0.03$  s,  $t = 0.06$  s,  $t = 0.09$  s,  $t = 0.12$  s and  $t = 0.15$  s.

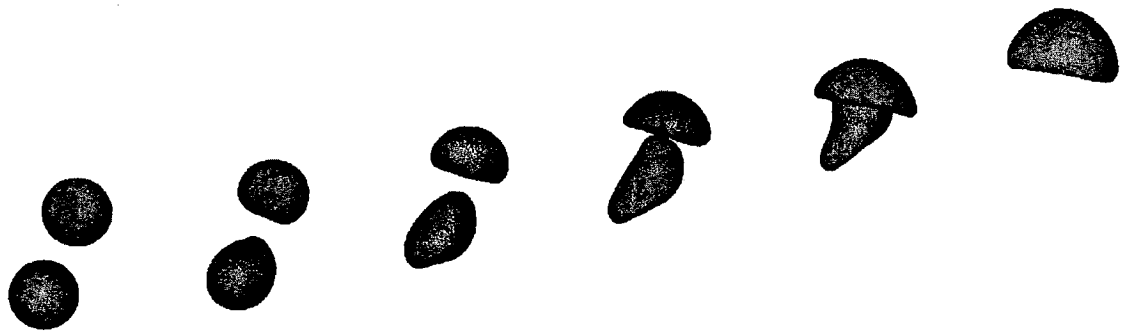


Fig. 16. Transient solution of the bubble coalescence in a continuous phase, the bubbles are not in-line, for  $t = 0.0$  s,  $t = 0.03$  s,  $t = 0.06$  s,  $t = 0.09$  s,  $t = 0.12$  s and  $t = 0.15$  s.

As in the previous example, the bubbles rise due to buoyancy forces. The nondimensional parameters are:  $Re = 55.75$ ,  $Fr = 1$ ,  $We = 4.6$ . For the continuous phase,  $\rho_f = 880 \text{ kg/m}^3$  and  $\mu_f = 0.0125 \text{ Ns/m}^2$ . For the larger bubble,  $D_1 = 4 \text{ mm}$ ,  $\rho_1 = 88 \text{ kg/m}^3$  and  $\mu_1 = 0.00125 \text{ Ns/m}^2$ , with  $Eo_1 = 4.6$ . Finally, for the smaller bubble,  $D_2 = 2 \text{ mm}$ ,  $\rho_2 = 176 \text{ kg/m}^3$  and  $\mu_2 = 0.0025 \text{ Ns/m}^2$ , with  $Eo_2 = 1.15$ . The surface tension coefficient for all interfaces is  $\sigma_I = 0.03 \text{ N/m}$ . The lengths and velocities were nondimensionalized using  $D_1 = 4 \text{ mm}$  and  $U = \sqrt{gD_1}$ , respectively. The grid used in this example was  $32 \times 32 \times 64$  cells.

Figure 13 shows the time evolution of the flow. It can be seen that the larger bubble undergoes a larger deformation than the smaller bubble, due to its larger Eötvös number. Figure 14 shows a small deflection in the trajectory of the smaller bubble due to the interaction with the larger bubble as it passes by.

## 6.6 Bubble coalescence

Another classical example of multi-fluid flows is the coalescence of two bubbles in a continuous phase. The two bubbles are positioned in-line at a distance of  $0.4\text{ mm}$  apart. The diameter of both bubbles is  $D = 2.6\text{ mm}$ , the velocities of each bubble are nondimensionalized using  $U = \sqrt{gD} = 0.15\text{ m/s}$ , the interfacial tension coefficient is  $\sigma_I = 5.8 \times 10^{-4}\text{ N/m}$ , and the nondimensional constants  $Re = 30$  and  $Eo = 100$  are the Reynolds and Eötvös numbers, respectively. For the continuous phase,  $\rho_f = 880\text{ kg/m}^3$ ,  $\mu_f = 0.0125\text{ Ns/m}^2$ , and for the bubbles,  $\rho_d = 440\text{ kg/m}^3$ ,  $\mu_d = 0.00625\text{ Ns/m}^2$ . Figure 15 shows the transient solution of the interface, with the coalescence of both bubbles, starting from the bubbles initially in-line.

The same flow parameters were used to simulate the rise of two bubbles that are initially not aligned. Figure 16 shows the three-dimensional rendering of the transient solution, in which the bottom bubble chases the top bubble until the coalescence occurs. This is due to the lower pressure close to the bottom of the top bubble. These results are in good agreement when compared with the numerical results obtained by Li Chen & Yuguo Li (1998) [6] and the experimental results obtained by Narayanan et. al. (1974) [16].

## 6.7 Two-fluid splashing drop

Splashing drops are good examples to illustrate the robustness of the free surface flow codes. In this particular case, a two-fluid splashing drop was simulated, whereby a drop falls into a container of a quiescent fluid of a different phase resulting in a splash.

The drop phase was taken to be less viscous and lighter than the continuous phase. The nondimensional parameters were given by:  $Re = 30$ ,  $Fr = 1$  and  $We = 50$ . For the drop phase, we set  $\rho_g = 440\text{ kg/m}^3$  and  $\mu_g = 0.00625\text{ Ns/m}^2$ ; for the continuous phase, we used  $\rho_f = 880\text{ kg/m}^3$  and  $\mu_f = 0.0125\text{ Ns/m}^2$ . The interfacial tension coefficient was  $\sigma_I = 0.001167\text{ N/m}$ , and the free surfaces are driven by surface tension forces, with the same coefficient. Again, we used the drop diameter  $D$  and the reference velocity  $U = \sqrt{gD}$  to nondimensionalize the lengths and velocities.

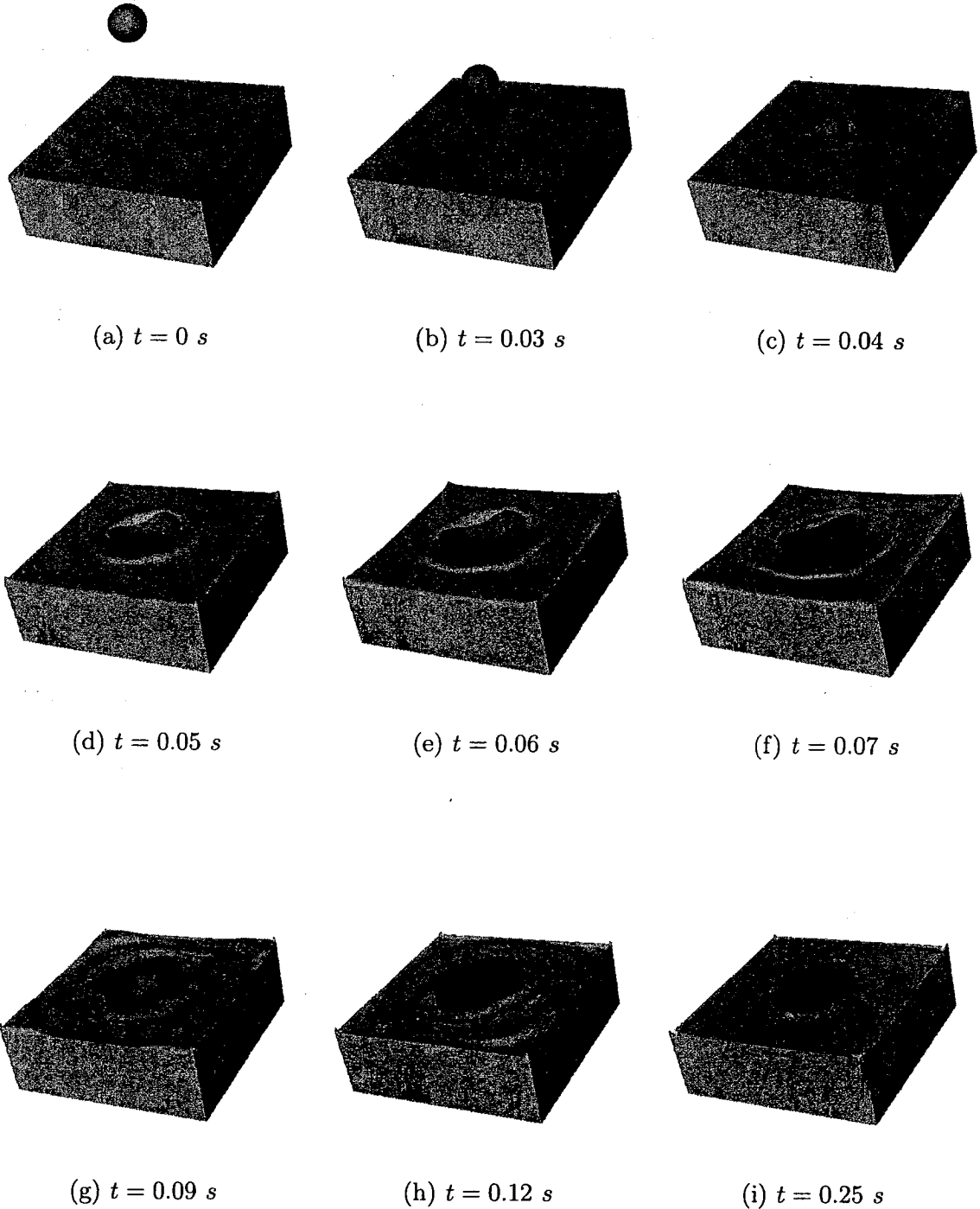


Fig. 17. Transient solution of the splashing drop falling over a free surface of a heavier and more viscous fluid.

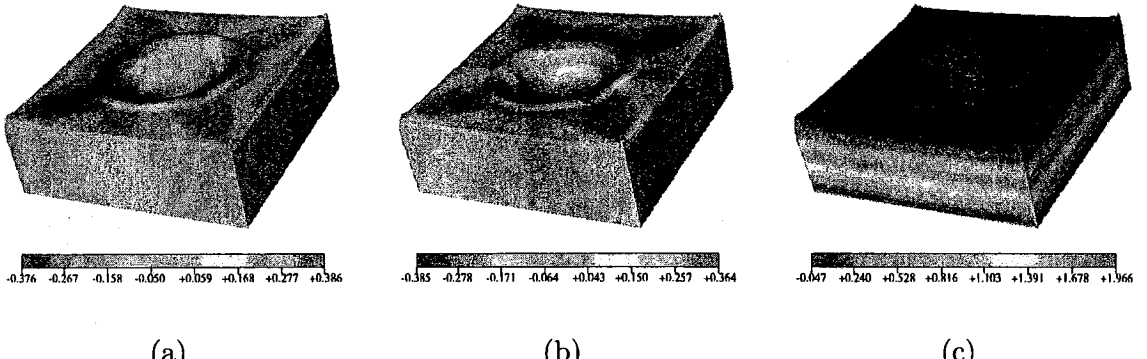


Fig. 18. Three-dimensional color scale rendering of the solution at time  $t = 0.06$  s; (a)  $x$  direction velocity; (b)  $y$  direction velocity; (c) pressure.

Figure 17 shows the transient solution of the flow in a  $40 \times 40 \times 40$  grid. In this figure we are able to observe the surface tension effects acting over the free surfaces. Figure 18 shows the rendering of the solution using pseudo-color to indicate velocity components and pressure over the free surfaces. Figure 18 displays the  $x$ -direction velocity, the  $y$ -direction velocity and the pressure at time  $t = 0.06$  s. We can see that the velocity field remains symmetric after the drop impact.

This simulation is an important indicator of the robustness of the code, where we can see the interaction between the free surfaces and the interface. The code has the capability to decide when fronts should be treated as free surfaces or as interfaces, using the information stored in its internal cellular representation.

## 7 Conclusions

In this work, a method for simulating incompressible multi-fluid flows with surface tension was described. This method was based on the GENSMAC-3D front-tracking method [28], using finite difference schemes to discretize the governing equations, as in [19]. Surface and interfacial tensions were considered, and the required curvature on the interface was computed by a technique of geometrical surface approximation [4,13,22,24].

A number of numerical simulations was used to validate the method presented

in this paper. The simulation of static bubbles showed good agreement with the analytic solution, with errors less than 1.2% indicating that the curvature calculation procedure is accurate. A numerical convergence test was performed indicating quadratic convergence of the curvature calculation.

A sessile drop simulation was also carried out to verify the accuracy of the surface tension approximation method. The results were compared with the analytic solution for the steady state axisymmetric case showing good agreement. Two types of simulations were performed. The first one shows small undulations over the free surface that are unphysical and due to the discretization of the domain. Since the surface tension method acts on the scale of a cell it cannot eliminate these undulations in scales smaller than a cell. Thus a geometric filter was developed. The filter, called TSUR-3D [23,24], smoothes the free surface and interfaces, while conserving the mass of the fluid. The second type of simulation was made with the TSUR-3D filter and shows that the filter has eliminated the undulations and so improving the accuracy of the solution.

In order to show the correct transfer between the surface energy and kinetic energy, a transient two-fluid oscillating bubble was simulated. The result was compared with the analytical expression for the frequency and the amplitude decay. This also showed reasonable agreement.

Rising bubbles immersed in a continuous phase are classical examples to corroborate any fluids code. Bubbles rising with low and moderate Reynolds numbers were simulated with good results, when compared with results in the literature [7,8]. The results showed small oscillations in the rising Reynolds number of the bubbles, occurring in coarse grids, and vanishing when the grid was subsequently refined. This effect is due to the fact that the bubble diameter is very small for the grid used, causing larger errors in the interfacial tension distribution and was essentially eliminated when the grid was refined. A three-fluid rising bubble simulation was also made to show the interaction between the fluids and the influence of the buoyancy forces on the flow. Bubble coalescences were simulated, with bubbles initially in-line and not in-line and the results were compared with numerical [6] and experimental [16] results of similar problems.

Finally, a two-fluid splashing drop was simulated to illustrate the robustness and applicability of the code to compute the interactions between free surfaces and interfaces. All these results together demonstrate that the new method can be used

to simulate a number of problems and to investigate many physical phenomena involving incompressible multi-fluid flows, including free surfaces.

## Acknowledgments

We thank the financial support given by the Brazilian agencies FAPESP (Fundação de Amparo a Pesquisa do Estado de São Paulo), grant 01/12623-5 and 00/03385-0, and CNPq (Conselho Nacional de Desenvolvimento Científico e Tecnológico), grant 460473/01-8.

## References

- [1] Amsden, A. A., Harlow, F. H. (1970). "The SMAC Method: a Numerical Technique for Calculating Incompressible Fluid Flows", Los Alamos Scientific Laboratory, Report LA-4370.
- [2] Armenio, V. (1997). "An improved MAC method (SIMAC)for unsteady high-Reynolds free surface flows". *International Journal for Numerical Methods in Fluids*, 24:185–214.
- [3] Brackbill, J. U., Kothe, D. B., Zemach, C. (1992). "A continuum method for modeling surface tension", *Journal of Computational Physics*, 100:335–354.
- [4] Castelo, A., Mangiavacchi, N. Cuminato, J. A., Fortuna, A. O., Oliveira, J. Tomé, M. F., McKee, S. (1999). "Surface Tension Implementation for GENSMAC2D Code", Proceedings of the 15th Brazilian Congress of Mechanical Engineering (COBEM), Águas de Lindóia - SP, CD-ROM.
- [5] Castelo, A., Tomé, M. F., César, C. N. L., McKee, S. and Cuminato, J. A. (2000). "Freeflow: An integrated simulation system for three-dimensional free surface flows". *Computing Visualization in Science*, 2: 199–210.
- [6] Li Chen & Yuguo Li (1998). "A numerical method for two-phase flow with an interface". *Environmental Modeling & Software*, 13:247–255.
- [7] Esmaeeli, A., Tryggvason, G. (1998). "Direct numerical simulations of bubbly flows. Part 1. Low Reynolds number arrays". *Journal of Fluid Mechanics*, 377:313–345.

[8] Esmaeeli, A., Tryggvason, G. (1999). "Direct numerical simulations of bubbly flows. Part 2. Moderate Reynolds number arrays". *Journal of Fluid Mechanics*, 385:325–358.

[9] Ferreira, V. G., Tomé, M. F., Mangiavacchi, N., Castelo, A., Cuminato, J. A., Fortuna, A. O., McKee, S. (2002) "High Order Upwinding and the Hydraulic Jump", *International Journal for Numerical Methods in Fluids*, 39:549–583.

[10] Glimm, J., Grove, J., Lindquist, B., McBryan, O. and Tryggvason, G. (1988) "The bifurcation of tracked scalar waves", *SIAM Journal on Scientific and Statistical Computing*, 9:61–79.

[11] Harlow, F. H. and Welch, J. E. (1965). "Numerical Calculation of Time-Dependent Viscous Incompressible Flow of Fluid with Free Surface". *Physics of Fluids*, 8(1):2182–2189.

[12] Hirt, C. W. and Nichols, B. D. (1981). "Volume of Fluid (VOF) method for the dynamics of free boundaries". *Journal of Computational Physics*, 39:201–235.

[13] Mangiavacchi, N., Castelo, A., Cuminato, J. A., Fortuna, A. O., Tomé, M. F., Nonato, L. G., McKee, S. (2000). "Numerical Simulation of Surface Tension Dominated Axisymmetric Free Surface Flows", Proceedings of ENCIT'2000, Porto Alegre - RS, CD-ROM.

[14] Mäntyla, M. (1988). "An Introduction to Solid Modeling", *Computer Science Press*, Rockville, Maryland.

[15] Miyata, H. (1986). "Finite difference simulation of breaking waves". *Journal of Computational Physics*, 65:179–214.

[16] Narayananam, S., Groossens, H. J., Kossen, N. W. F. (1974). "Coalescence of two bubbles rising in line at low Reynolds number", *Chemical Engineering Science*, 29:2071–2082.

[17] Nichols, B. D., Hirt, C. W. and Hotchkiss, R. S. (1988). "SOLA-VOF: a solution algorithm for transient fluid flows with multiple free boundaries". Los Alamos Scientific Laboratory, Report LA-8355.

[18] Osher, S. and Sethian, J. A. (1988). "Fronts propagating with curvature-dependent speed: Algorithms based on Hamilton-Jacobi formulations", *Journal of Computational Physics*, 79:12–49.

[19] Santos, F. L. P., Mangiavacchi, N., Castelo, A., Tomé, M. F., Ferreira, V. G., Cuminato, J. A. (2001) "Numerical Simulation of Multi-phase Flows Using

the FreeFlow-2D System", Proceedings of 16th Brazilian Congress of Mechanical Engineering (COBEM), Uberlândia - MG, CD-ROM.

- [20] Sethian, J. A. (1996). "Level Set Methods", *Cambridge University Press*.
- [21] Sethian, J. A. (1999). "Level Set Methods and Fast Marching Methods", *Cambridge University Press*.
- [22] Sousa, F. S., Mangiavacchi, N., Castelo, A., Nonato, L. G., Tomé, M. F., Cuminato, J. A. (2001). "Simulation of 3D Free-surface Flows with Surface Tension", Proceedings of 16th Brazilian Congress of Mechanical Engineering (COBEM), Uberlândia - MG, CD-ROM.
- [23] Sousa, F. S., Mangiavacchi, N., Castelo, A., Nonato, L. G., Tomé, M. F., Cuminato, J. A. (2001). "A mass conserving filter for the simulation of 3D free surface flows with surface tension", Proceedings of 22nd Iberian Latin-American Congress on Computational Methods in Engineering (CILAMCE), Campinas - SP, CD-ROM.
- [24] Sousa, F. S., Mangiavacchi, N., Castelo, A., Nonato, L. G., Tomé, M. F., Cuminato, J. A. (2002). "Numerical Simulations of 3D Free-surface Flows with Surface Tension", Proceedings 5th International Meeting on High Performance Computing for Computational Science (VECPAR), 1:225-238.
- [25] Sussman, M., Smereka, P., Osher, S. (1994). "A level set approach for computing solutions to incompressible two-phase flow", *Journal of Computational Physics*, 114:146–159.
- [26] Tomé, M. F., McKee, S. (1994). "GENSMAC: A Comp. Marker-and-Cell Method for Free Surface Flows in General Domains". *Journal of Computational Physics*, 110(1):171–189.
- [27] Tomé, M. F., Castelo, A., Murakami, J., Cuminato, J. A., Minghim, R., Oliveira, M. C. F., Mangiavacchi, N., and McKee, S., (2000). "Numerical Simulation of Axisymmetric Free Surface Flows", *Journal of Computational Physics*, 157:441–472.
- [28] Tomé, M. F., Castelo, A., Cuminato, J. A., Mangiavacchi, N., and McKee, S., (2001). "GENSMAC3D: A Numerical Method for Solving Unsteady Three-dimensional Free Surface Flows", *International Journal for Numerical Methods in Fluids*, 37(7):747–796.
- [29] Tryggvason, G., Bunner, B., Ebrat, O., and Tauber, W., (1998). "Computations of Multiphase Flows by a Finite Difference/Front Tracking Method. I Multi-Fluid Flows", In: *29th Computational Fluid Dynamics. Lecture Series 1998-03. Von Karman Institute for Fluid Dynamics*.

[30] Tryggvason, G., Esmaeeli, A., Mortazavi, S., Han, J., and Homma, S., (1998). "Computations of Multiphase Flows by a Finite Difference/Front Tracking Method. II Applications", In: *29th Computational Fluid Dynamics. Lecture Series 1998-03. Von Karman Institute for Fluid Dynamics*.

[31] Tryggvason, G., Juric, D., Che, J., Nobari, M. R. H., and Nas, S. (1998). "Computations of Multiphase Flows by a Finite Difference/Front Tracking Method. III Variable Surface Tension and Phase Change", In: *29th Computational Fluid Dynamics. Lecture Series 1998-03. Von Karman Institute for Fluid Dynamics*.

[32] Unverdi, S. O., Tryggvason, G. (1991). "A Front-Tracking Method for Viscous Incompressible Multi-Fluid Flows". *Journal of Computational Physics*, 100:25–27.

[33] Veldman, A. E. P. and Vogels, M. E. (1984). "Axisymmetric liquid splashing under low gravity conditions". *Acta Astronautica*, 11:641–649.

[34] Viecelli, J. A. (1971). "A computing method for incompressible flows bounded by moving walls". *Journal of Computational Physics*, 65,179–214.

[35] Welch, J. R., Harlow, F. H., Shannon, J. P., Daly, B. J. (1965). "The MAC Method", Los Alamos Scientific Laboratory, Report LA-3425.

# NOTAS DO ICMC

## SÉRIE COMPUTAÇÃO

072/2003 MANGIAVACCHI, N.; CASTELO FILHO, A.; TOMÉ, M.F.; CUMINATO, J.A.; OLIVEIRA, M.L.B.; McKEE, S. – A numerical technique for including surface tension effects for axisymmetric and planar flows using the gnsmac method.

071/2003 TOMÉ, M.F.; GROSSI, L.; CASTELO, A.; CUMINATO, J.A.; MANGIAVACCHI, N.; FERREIRA, V.G.; SOUSA, F.S.; McKEE, S. – A numerical method for solving three-dimensional generalized Newtonian free surface flows.

070/2003 SANTOS, F.L.P.; MANGIAVACCHI, N.; CASTELO, A.; TOMÉ, M.F.; CUMINATO, J.A. – A novel technique for free surface 2D multiphase flows.

069/2003 VIANNA, A.C.G.; ARENALES, M.N.; GRAMANI, M.C.N. – Two-stage and constrained two-dimensional guillotine cutting problems.

068/2003 ARAUJO, S.A.; ARENALES, M.N.; CLARK, A.R. – A lot-sizing and scheduling problem in a foundry.

067/2003 ARAUJO, S.A.; ARENALES, M.N. – Dimensionamento de lotes e programação do forno numa fundição automatizada de porte médio.

066/2002 VALERIO NETTO, A.; OLIVEIRA, M.C.F. – Industrial application trends and market perspectives for virtual reality and visual simulation.

065/2002 VALERIO NETTO, A.; OLIVEIRA, M.C.F. – Desenvolvimento de um protótipo de um torno CNC utilizando realidade virtual.

064/2002 MARQUES, F.P.; ARENALES, M.N. - O problema da mochila compartimentada e aplicações.

063/2001 TOMÉ, M F; MANGIAVACHI, N; CUMINATO, J A; CASTELO, A – A marker-and-cell technique for simulating unsteady viscoelastic free surface flows.